NEW FRONTIERS IN CHEMISTRY
New Front. Chem.

(*former Annals of West University of Timişoara – Series of Chemistry*)

(2014) Volume 23, Number (Issue) 2, pp. 79-147

Ordinary Issue

TABLE OF CONTENTS

PUBLISHER:
Universitatea de Vest
din Timişoara

NEW FRONTIERS IN CHEMISTRY: METADATA

New Frontiers in Chemistry (New Front. Chem.) is an open-access fee-free peer-review international academic journal addressing the modern trends and frontiers in fundamental, applicative and multidisciplinary chemistry, paralleling the ever-expanding chemical data, methods, and compounds available and continuously produced, towards cross fertilizing the multidisciplinary ideas as coming from Chemistry combined with Mathematics, the Natural and Applied sciences (Physics, Biology, Medicine, Agriculture, Environmental, Engineering), and beyond.

NEW FRONTIERS IN CHEMISTRY
(NEW FRONT. CHEM.)
is published biannually by

West University of Timișoara
Blvd. V. Parvan 4
Timisoara 300223, ROMANIA
E-mail: newfrontchem@iqstorm.ro
Web: www.newfrontchem.iqstorm.ro

ISSN 2393 – 2171
ISSN-L 2393 – 2171

Subscription Price per Volume
Electronic: open access   Print: on demand by above email address

Additional color graphics is available in the e-version of this Journal

NEW FRONTIERS IN CHEMISTRY: EDITORS

Editorial Board:

Advisory Editors
(from members of Biology-Chemistry Department of West University of Timișoara):

VASILE OSTAFE (Biochemistry, Chromatography, Environmental Chemistry)
IONEL CIUCANU (Instrumental Techniques for Analytical Chemistry)
ADRIANA ISVORAN (Biophysics, Bioinformatics)
MIHAI V. PUTZ (Nanochemistry, Quantum Chemistry)
TITUS VLASE (Thermal Analysis, Chemical Kinetics, Chemistry of Solid State)
GABRIELA VLASE (Inorganic Chemistry, Thermal Analysis)
OTILIA BIZEREA (Inorganic Chemistry)
GABRIELA PREDA (Organic Chemistry, Catalysis)
CONSTANTIN BOLCU (Organic Chemistry, Polymers)
VLAD CHIRIAC (General and Analytical Chemistry, Electrochemistry)
DANA VLASCICI (Analytical Chemistry)
DANIELA DASCALU (Thermodynamics and Chemical Statistics)
CORINA DUDA-SEIMAN (QSAR, Organic Chemistry, Medicinal Chemistry)
LAURA PITULICE (Environmental Chemistry)
HORIA POPOVICI (Colloidal Chemistry, Analytical Chemistry)
BEATRICE VLAD-OROS (Chemical and Enzyme Kinetics)
MARIANA ALBULESCU (Organic Chemistry, Natural Compounds)
DORINA MODRA (Organic Chemistry)
MIRCEA SELEGEAN (Biotechnologies)
NICOLETA IANOVIC (Aerobiology, Plant Physiology)

Honorary Editors
(as Doctor Honoris Causa of WUT/CBG & Formers Editors and Developers of Annals of West University of Timișoara – Series Chem.):

ALEXANDRU BALABAN (Texas A&M University at Galveston, USA, & Romanian Academy, Romania)
HAGEN KLEINERT (Berlin Free University, Germany)
KATLEEN SWALLOW (Merrimack College, USA)
GABOR NÁRÁY-SZABÓ ("Lorand Eőtvős" University Budapest, Hungary)
EUGEN SEGAL (University of Bucharest, Romanian Academy, Romania)
VICTOR EMANUEL SAHINI (PolytechnicBucharest, Romanian Academy, Romania)
MARIUS ANDRUH (Romanian Academy, Bucharest)
ZENO SIMON (Romanian Academy, Romania)
ADRIAN CHIRIAC (West University of Timisoara, Romania)
MIRCEA MRACEC (West University of Timisoara, Romania)
VASILE OSTAFE (West University of Timisoara, Romania)
NICOLAE BONCIOCAT (†, Babes-Bolyai University, Cluj-Napoca, Romania)
ALAN R. KATRITZKY (†, University of Florida, Gainesville, USA)

NEW FRONT. CHEM. (**2014**)
Volume 23, Number 2, pp. 79-89
ISSN 2393-2171; ISSN-L 2393-2171
© West University of Timișoara

Former: Ann. West Univ. Timisoara – Series Chem.
ISSN: 1224-9513

Article

INTERACTION OF A COPPER ATOM WITH RDX

Lemi Türker[♣]

Middle East Technical University, Department of Chemistry, 06800, Ankara, TURKEY

ABSTRACT

The effect of a copper atom on RDX molecule is considered within the constraints of density functional theory, at the level of UB3LYP/6-31++G(d,p), UB3LYP/LANL2DZ and UB3LYP/SBKJC. in all the cases, one of the nitro groups is distorted and nitrogen-oxygen bond is broken. the charge distribution indicates that Cu atom transfers some of its electron population to RDX, especially to atoms of the distorted NO_2 moiety. this partial redox process is supported by all the basis sets employed in the calculations. the structural and energetic properties of RDX in the presence of copper atom are discussed.

Keywords: Hexamine, RDX, 1,3,5-trinitrohexahydro-*sym*-triazine, Explosives, Copper, DFT calculations.

1. INTRODUCTION

Cyclotrimethylene trinitramine or 1,3,5-trinitrohexahydro-*sym*-triazine (RDX) [1] is an important explosive which has been in use for long. The most stable crystalline structure of RDX belongs to α–RDX. It is one of the most effective energetic materials with applications ranging from explosives and propellants [2]. RDX is mainly obtained in the industry by direct nitrolysis process (Woolwich) in which hexamethylene tetramine is directly treated with a large excess of strong HNO_3 [1,3-5] at a temperature of 20-25 °C. On the other hand, in the Bachman (Combination Process) process, which is also an industrial process for RDX, the reaction mixture contains HNO_3, NH_4NO_3, acetic anhydride and acetic acid in addition to hexamine [1,3,5].

Besides the experimental studies on RDX, there are some computational studies on its reaction mechanism [6], conformations and bond dissociation energies [7, 8] and gas-phase structure [9]. De Paz and Ciller [10] used Stewart's new semi–empirical method MNDO–PM3 (PM3) for the calculation of gas phase heat of formation of RDX. Catoire et al.,[11]

[♣] Correspondent author: Tel:+90 312 2103244, Fax:+90 312 2103200, E-mail: lturker@metu.edu.tr presented the thermochemical properties of RDX by means of the Density Functional Theory (DFT). In the study of Rice et al., [12], $\Delta H_f^o{}_{(RDX)}$ was calculated by using an isodesmic reaction and DFT method (B3LYP/6–31G(d) level). The value was obtained as 52.8 kcal/mol which was ~ 7 kcal/mol greater than the experimental value. Whereas, in the same study $\Delta H_f^o{}_{(RDX)}$ was calculated to be 45.3 kcal/mol by using atom–equivalent method (with a difference of –0.5 kcal/mol from the experimental value) and that of solid state has been found to be 20.8 kcal/mol (with a difference of +1.9 kcal/mol from the experimental value).

On the other hand, there exist some experimental and theoretical studies on RDX-metal interactions. Density functional theory study of interactions of cyclotrimethylene trinitramine (RDX) with metal-organic framework was reported [13]. Note that copper is one of the metals widely used (either alone or in the form of certain alloys) in ammunitions.

A mathematical flow model is described for one-dimensional detonations in mixtures of high explosives with small inert metal particles. The model and observed detonation velocities for mixtures of RDX and Cu are used to calibrate the assumed equation of state constant as a function of the particle mass fraction [14]. Methods to investigate the igniter /propellant interaction were reported. The tests were performed with black powder and some RDX/metal mixtures including copper [15]. Influence of metal substrates on the detection of explosive residues with laser-induced breakdown spectroscopy was studied [16]. It is demonstrated that despite the strong spectral variation in cyclotrimethylenetrinitramine (RDX) residues applied to various metal substrates, classification of the RDX residue independent of substrate type is feasible.

In the present study, effect of a copper atom on RDX molecule is considered within the constraints of DFT.

2. METHOD

The initial structure optimizations of all the structures leading to energy minima were achieved by using MM2 (molecular mechanics) method followed by semi-empirical PM3 self-consistent fields molecular orbital (SCF MO) method [17,18] at the restricted level [19]. Then, structure optimizations were achieved by using various restricted Hartree-Fock (RHF) methods successively and finally optimizing within the framework of density functional theory (DFT, UB3LYP) [20,21] using basis sets 6-31++G(d,p), LANL2DZ and SBKJC. Note that the exchange term of B3LYP consists of hybrid Hartree–Fock and local spin density (LSD) exchange functions with Becke's gradient correlation to LSD exchange [22,23]. The correlation term of B3LYP consists of the Vosko, Wilk, Nusair (VWN3) local correlation functional [23] and Lee, Yang, Parr (LYP) correlation correction functional [24].

For each set of calculations, vibrational analyses were done (using the same basis set employed in the corresponding structure optimization). The normal mode analysis for each structure yielded no imaginary frequencies for the 3N−6 vibrational degrees of freedom, where N is the number of atoms in the system. This indicates that the structure of each molecule corresponds to at least one local minimum on the potential energy surface. All these computations were performed by using the Spartan 06 [25] package program.

3. RESULTS AND DISCUSSIONS

Elemental copper is characterized with ....3d104s1 electronic configuration in the ground state [26]. The presence of an unpaired electron may cause Cu atom to interact with electron population of some nearby molecules.

3.1. Geometries

As seen in Figure 1 the structure optimizations all show that the presence of Cu atom in the vicinity of RDX molecule causes appreciable elongation of one of nitrogen-oxygen bonds of nitramine group. However, UB3LYP/6-32++G(d,p) type calculation yields a structure (1a, Conformer I) different from the structures obtained by using LANL2DZ (1c) and SBKJC (1d) basis sets. Structure 1b (conformer II) is obtained when structure 1c is reoptimized with UB3LYP/6-32++G(d,p) method. Structures 1a and 1b are two conformers in which nitramine groups occupy different equatorial and axial positions. Bond angles around amine nitrogen linked to NO_2 groups are in between 114°-123° in 1a and 117°-125° in 1b indicating nearly planar arrangement. In 1a one axial and one equatorial NO_2 groups exist whereas in 1b two axial NO_2 exist (see Figure 1). On the other hand, the reverse sequence of optimization process; namely UB3LYP/LANL2DZ optimization of UB3LYP/6-31++G(d,p) optimized structure yielded, the originally UB3LYP/LANL2DZ optimized structure in appearance.

In appearance, LANL2DZ and SBKJC basis sets yield similar structures, similar to conformer II (two nitro groups are axial). Bond angles about the amine nitrogen linked to distorted NO_2 group are in between 116°-125° in 1c and 117°-125° in 1d. Figure 2 depicts bond lengths of the structures obtained by using different basis sets.

Figure 1: RDX+Cu structure optimized by using different basis sets

UB3LYP/6-31++G(d,p)
Conformer (I) **1a**

UB3LYP/6-31++G(d,p)
Conformer (II) **1b**

UB3LYP/SBKJC
1c

UB3LYP/LANL2DZ
1d

Figure 2: Bond lengths (10^{-10} m) in the optimized RDX+Cu system considered

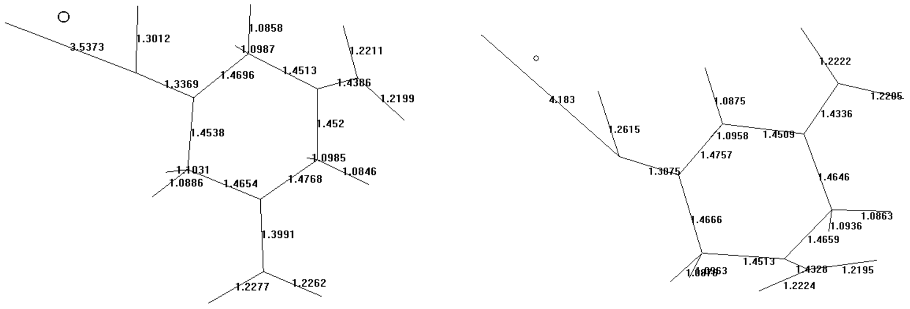

UB3LYP/6-31++G(d,p)
Conformer (I)

UB3LYP/6-31++G(d,p)
Conformer (II)

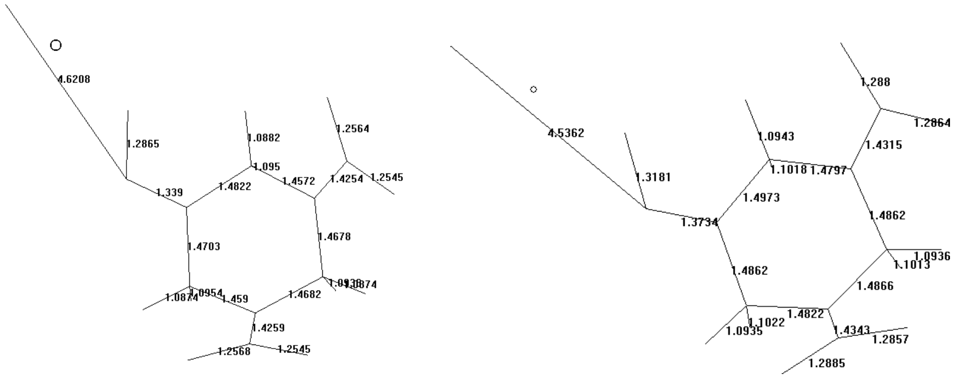

UB3LYP/LANL2DZ

UB3LYP/SBKJC

Whereas, Figure 3 shows similar data for RDX. As seen there the optimization with LANL2DZ and SBKJC basis sets yield similar RDX structures, in which two of the nitro groups are on the same side (occupy axial positions), contrary to the case of 6-31++G(d,p) basis set. Note that 6-31G(d,p) basis sets and its diffuse form (eg; 6-31++G(d,p)) are available for elements H-Kr [27]. The LANL2DZ basis set is especially for the transition metal complexes (including Cu) [27-29]. The SBKJC is available for heavy atoms, Rb and heavier [27]. The bond lengths in conformers I and II are generally similar, except the N-O bond nearby the copper atom. In conformer II the elongated bond (actually nitrogen-oxygen distance) is 4.18 10^{-10} m whereas 3.53 10^{-10} m in conformer I. The LANL2DZ and SBKJC based optimizations yield the length of this bond as 4.62 10^{-10} m and 4.53 10^{-10} m, respectively. All these data indicate that copper atom causes cleavage of this particular bond. The distance between the Cu atom and other oxygen of the nitro group varies between 1.85-1.90 10^{-10} m depending on the type of basis set used. Nitramine bonds in RDX are in between 1.39-1.43 10^{-10} m (UB3LYP/6-31++G(d,p)); 1.41 10^{-10} m (UB3LYP/LANL2DZ); 1.39-1.43 10^{-10} m (UB3LYP/SBKJC). Whereas, in the presence of Cu atom, the nitramine bond incident to the distorted NO_2 group is 1.33 10^{-10} m, which means some electron population has been transferred from amine nitrogen to the nitro group perturbed by Cu. Table 1 shows the dipole moments and some distances to Cu atom in the structures considered.

Figure 3: Bond lengths (10^{-10} m) of RDX molecule in the optimized structure

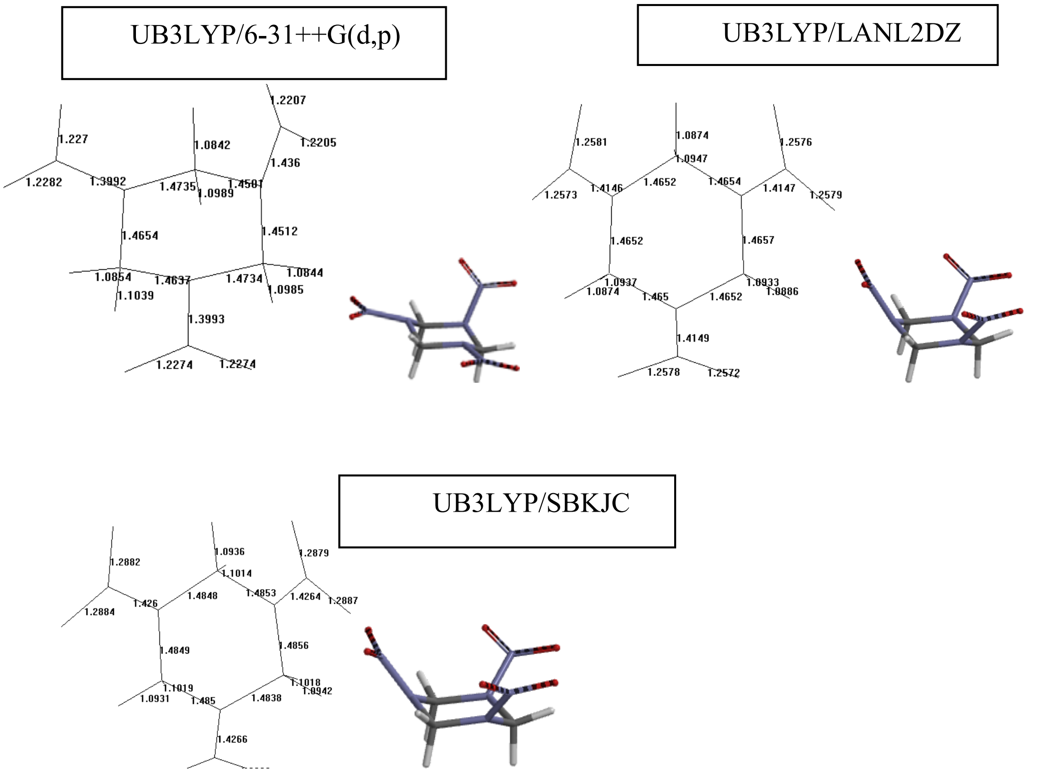

Table 1: Dipole moments and Cu-O and Cu-N distances of the optimized structure

Method	**Dipole moment**	**Cu-O***	**Cu-N**	**Cu-O**
UB3LYP/6-31++G(d,p) Conformer **I** (**1a**)	2.93	1.71	2.02	1.87
UB3LYP/6-31++G(d,p) Conformer **II** (**1b**)	13.54	1.70	2.61	1.85
UB3LYP/LANL2DZ	162.36	1.78	2.89	1.90
UB3LYP/SBKJC	94.44	1.75	2.84	1.86

Dipole moments in Debye, distances in 10^{-10} m. * Oxygen of the broken bond.

3.2. Charges

Figure 4 shows the electrostatic charge distribution on the optimized structures containing Cu atom. Two of the nitramine groups have amine nitrogen atoms possessing negative charge development. Whereas, the amine nitrogen linked to the distorted NO_2 group has positive charge accumulation. In each case, the copper atom acquires certain positive charge. Therefore, some electron population from the amine nitrogen and the copper atom should have been delivered to the nitrogen of the distorted NO_2 group. Indeed, negative charge develops on all the atoms of the distorted NO_2 group. So, the copper atom is oxidized whereas the distorted nitro group is reduced (partial oxidation and reduction). The distorted NO_2 group should have some partial resemblance to NO_2- group. Adjacent negative charges on the atoms of the distorted NO_2 group causes the N-O bond elongation and thus its cleavage. However, the charge distribution over the RDX moiety varies depending on the basis set employed (see Figure 4). So, conformers I and II have dipole moments possessing similar directional orientation whereas LANL2DZ and SBKJC based-optimized structures have oppositely oriented dipole moments to the previous two cases (see Figure 1). Also note that SBKJC based-optimized structure has some unusually high (in absolute values) charges on certain sites.

Figure 4: The electrostatic charges on the optimized RDX+Cu system

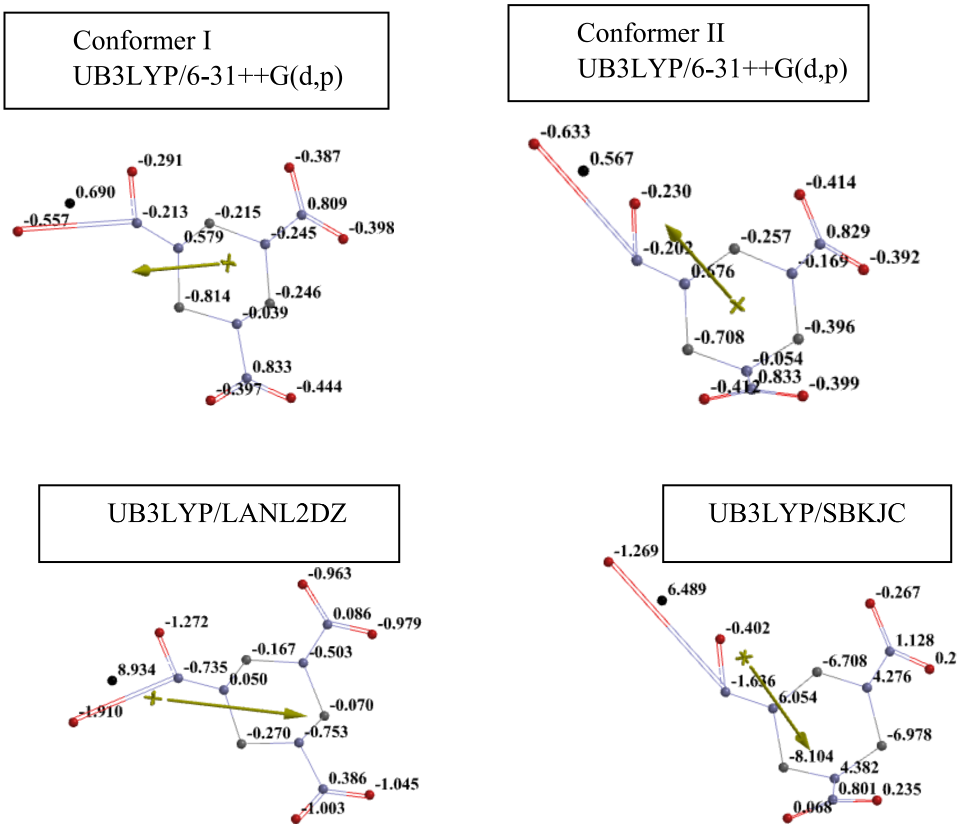

3.3. Energies

Table 2 shows the zero point energies (ZPE) and the corrected total energies (Ecorr) of the structures shown in Figure 1. As seen in Table 2 conformer I is more stable than conformer II. Note that both of them are the yield of UB3LYP/6-31++G(d,p) optimization. The single point calculation on the structure obtained by UB3LYP/LANL2DZ optimized structure, namely UB3LYP/6-31++G(d,p)//UB3LYP/LANL2DZ yields corrected total energy value less negative (Table 2, 5th energy value) than the respective energies of conformers I and II. Therefore, 6-31++G(d,p) basis set results in more stable optimized structure for conformer I. On the other hand, UB3LYP/LANL2DZ// UB3LYP/6-31++G(d,p) calculation (on conformer I yields less negative corrected total energy than UB3LYP/LANL2DZ (6th and 3rd energy values, respectively). Similar calculation on conformer II also yields less negative energy (7th and 3rd energy values, respectively). When the energies 6th and 7th are considered, LANL2DZ basis set results yields more stable conformer II than conformer I.

Table 2: ZPE and corrected total energies of the structures considered

Optimization method	**ZPE**	**E_{corr}**
UB3LYP/6-31++G(d,p) Conformer **I**	367.79	-6662465.16
UB3LYP/6-31++G(d,p) Conformer **II**	368.51	-6662439.55
UB3LYP/LANL2DZ	364.13	-2869899.11
UB3LYP/SBKJC	358.9	-975390.06
UB3LYP/6-31++G(d,p) //UB3LYP/LANL2DZ	362.58	-6662407.62
UB3LYP/LANL2DZ// UB3LYP/ 6-31++G(d,p) Conformer **I**	367.66	-2869811.37
UB3LYP/LANL2DZ// UB3LYP/ 6-31++G(d,p) Conformer **II**	369.2	-2869846.97

Energies in kJ/mol.

3.4. Molecular orbital energies

Figure 5 shows the molecular orbital energy spectra of the system. Conformer I possesses more condensed spacing of the lower lying occupied molecular orbital energy levels compared to conformer II. Consequently, it is more stable than the later one. Stereochemically, conformer I has one equatorial and one axial nitramine groups which should be more stable than conformer II with two axial groups. Note that one amine nitrogen has a nearly planar form in all the structures. Conformer I and II are characterized with large HOMO-LUMO energy separation (UB3LYP/6-31++G(d,p)). So they should be rather insensitive systems, because sensitivity (impact) is claimed to be associated with existence of closely spaced frontier molecular orbitals (FMO) namely the HOMO and LUMO [30]. On the contrary, UB3LYP/LANL2DZ and UB3LYP/SBKJC based calculations result relatively much closely spaced FMOs. Table 3 shows the FMO energies and interfrontier energy gaps ($\Delta\varepsilon=\varepsilon_{LUMO}-\varepsilon_{HOMO}$) of the systems considered.

Note that some of them are α- and some β-type orbitals because the composite system is an open shell due to unpaired electron of Cu atom. Table 4 contains similar data for RDX molecule. Comparison of the data in Tables 3 and 4 shows that Cu atom raises up the FMOs of RDX in the cases of UB3LYP/6-31++G(d,p) and UB3LYP/LANL2DZ but lowers when UB3LYP/SBKJC type calculations considered.

Figure 5: Molecular orbital energies of the system. a) UB3LYP/6-31++G(d,p) Conformer I; b) UB3LYP/6-31++G(d,p) ConformerII; c) UB3LYP/SBKJC; d) UB3LYP/LANL2DZ

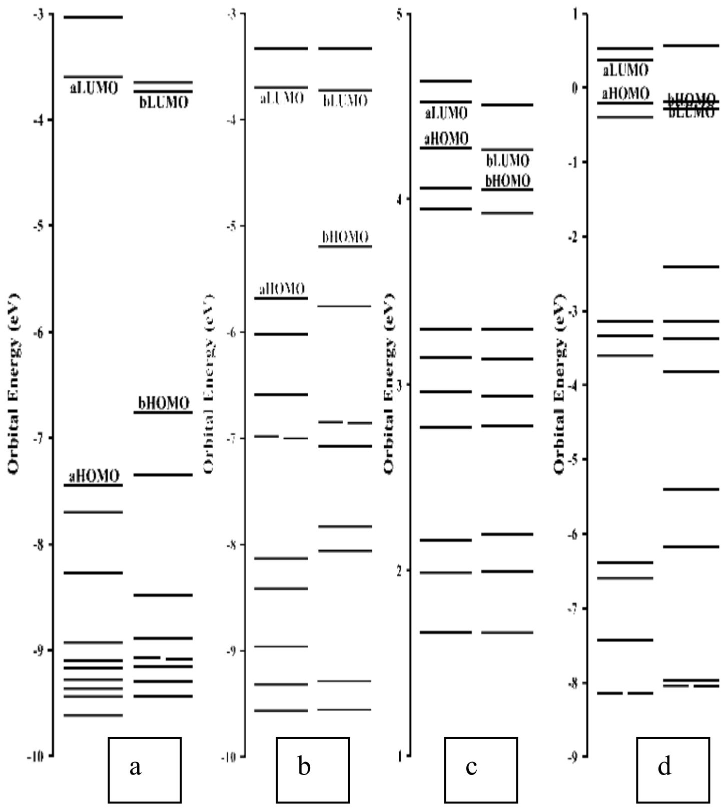

As seen in Figure 6 the HOMO and LUMO of conformer I and II (UB3LYP/6-31++G(d,p)) spread not only the nitramine group but over Cu atom as well. The d-atomic orbitals of Cu atom also contribute the LUMO. Cu atom denotes some electron population to the nitrogen atom and maybe accepting some from oxygen atoms into its empty d-orbitals.

Whereas, contribution to HOMO is little or nil in the cases of LANL2DZ and SBKJC basis sets, respectively. So UB3LYP/6-31++G(d,p) calculations represents a different picture from the others.

Table 3: The frontier molecular orbitals and interfrontier energy gaps of the structures considered

Optimization method	HOMO	LUMO	Δε
UB3LYP/6-31++G(d,p) Conformer **I**	-6.8 β	3.7 β	10.5
UB3LYP/6-31++G(d,p) Conformer **II**	-5.2 β	-3.7 β	1.5
UB3LYP/LANL2DZ	-0.2 α	-0.2 β	0
UB3LYP/SBKJC	4.3 α	4.3 α	0

Energies in eV. α and β stand for alpha and beta type orbitals. $\Delta\varepsilon = \varepsilon_{LUMO} - \varepsilon_{HOMO}$.

Table 4: The frontier molecular orbital energies and interfrontier energy gap of RDX

Optimization Method	HOMO	LUMO	Δε
UB3LYP/631++G(d,p)	-8.87	-2.89	5.98
UB3LYP/LANL2DZ	-8.65	-3.02	5.63
UB3LYP/SBKJC	4.57	4.57	0

Energies in eV. $\Delta\varepsilon = \varepsilon_{LUMO} - \varepsilon_{HOMO}$

Figure 6: The HOMO and LUMO patterns of the optimized system (the functional is UB3LYP)

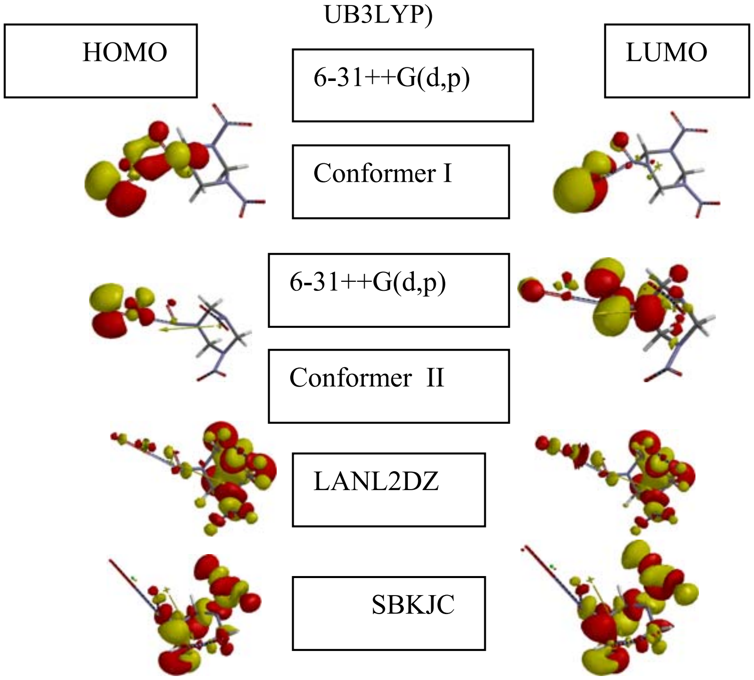

4. CONCLUSION

The present DFT study indicates that copper atom interacts with RDX molecule (in vacuum conditions), causing elongation of the nitrogen-oxygen bond of one of NO_2 groups. The elongation occurs whatever the basis set used (6-31++G(d,p), LANL2DZ or SBKJC) and it is so much that the bond cleaves. Moreover, the charge development indicates that Cu atom transfers some of electron population to RDX moiety. As a conjecture, in the solid phase this effect of Cu should be enhanced and change some ballistic properties of RDX and may cause some drastic results, at least, the shelf-life of RDX should be affected.

REFERENCES

1. Agrawal JP. High Energy Materials, Propellants,Explosives and Pyrotechnics, Wiley-VCH: Weinheim, 2010.
2. Zhu W , Xiao J , Zhu W , Xiao H , Molecular dynamics simulations of RDX and RDX-based plastic-bonded explosives, J. Hazard. Mater, **2009**, 164, 1082-1088.
3. Agrawal JP, Hodgson RD. Organic Chemistry of Explosives, Wiley: Sussex, 2007.
4. Fordham S. High Explosives and Propellants, Pergamon: Oxford, 1980.
5. Ledgard J. The Preparotory Manual of Explosives, J.B.Ledgard, USA, 2007.
6. Swadley MJ, Li T. Reaction mechanism of 1,3,5-trinitro-s-triazine (RDX) deciphered by density functional theory**,** J. Chem. Theory Comput. **2007**, 3, 505-513.
7. Harris NJ, Lammertsma K. *Ab initio* density functional computations of conformations and bond dissociation energies for hexahydro-1,3,5-trinitro-1,3,5-triazine, J. Am. Chem. Soc. **1997,** 119, 6583-6589.
8. Rice BM, Chabalowski CF. *Ab initio* and nonlocal density functional study of 1,3,5-trinitro-*s*-triazine (RDX) conformers, J. Phys. Chem. A **1997**, 101, 8720-8726.
9. Vladimiroff T, Rice BM. Reinvestigation of the gas-phase structure of RDX using Density functional theory predictions of electron-scattering intensities, J. Phys. Chem. A, **2002**, 106, 10437-10443.
10. De Paz J–LG, Ciller J. On the use of AMI and PM3 methods on energetic compounds, Propell Explos Pyrotech, **1993**, 18, 33-40.
11. Osmont A, Catoire L, Gökalp I, Yang V. *Ab initio* quantum chemical predictions of enthalpies of formation, heat capacities, and entropies of gas-phase energetic compounds, Combust Flame, **2007**, 151, 262-273.
12. Rice BM, Pai SV, Hare J. Predicting heats of, formation of energetic materials using Quantum mechanical calculations, Combust Flame, **1999**,118, 445-458.
13. Scott MA, Petrova T, Hill F, Leszczynski J. Density functional theory study of interactions of cyclotrimethylene trinitramine (RDX) and triacetone triperoxide (TATP) with metal-organic framework (IRMOF-1(Be)), Structural Chemistry, **2012**, 23(4), 1143-1154.
14. Ausherman DR, McKinnon CN, Jr., Detonation hydrodynamics for condensed explosives With inert additives, Astronautica Acta, **1970**, 15(5-6), 439-52.
15. Weiser V, Kelzenberg S, Knapp S, Roth E. Methods to investigate the igniter/propellant interaction, International Annual Conference of ICT , 2012, 43rd (Energetic Materials), **2012**, 69/1-69/10.

16. Gottfried JL. Influence of metal substrates on the detection of explosive residues with laser-Induced breakdown spectroscopy, Applied Optics, **2013**, 52(4), B10-B19.
17. Stewart JJP. Optimization of parameters for semi empirical methods I, Method. J. Comput. Chem. **1989**, 10, 209–220.
18. Stewart JJP. 1989. Optimization of parameters for semi empirical methods II, Appl. J. Comput. Chem.,**1989**, 10, 221–264.
19. Leach AR. Molecular Modeling, Longman: Essex, UK, 1997.
20. Kohn W, Sham LJ. Self-consistent equations including exchange and correlation effects. Phys. Rev., **1965**, 140, 1133–1138.
21. Parr RG, Yang W. Density Functional Theory of Atoms and Molecules, Oxford University Press: London, 1989.
22. Becke AD. Density-functional exchange-energy approximation with correct asymptotic behavior. Phys. Rev. A, **1988**, 38, 3098–3100.
23. Vosko SH, Vilk L, Nusair M. Accurate spin-dependent electron liquid correlation energies for local spin density calculations: A critical analysis. Can. J. Phys., **1980**, 58, 1200–1211.
24. Lee C, Yang W, Parr RG. Development of the Colle–Salvetti correlation energy formula into a functional of the electron density. Phys. Rev. B, **1988**, 37, 785–789.
25. SPARTAN 06. Wavefunction Inc., Irvine CA, USA, **2006**.
26. Durant PJ, Durant B. Introduction to Advanced Inorganic Chemistry, Longman: London, 1970**.**
27. Hehre WJ. A Guide to Molecular Mechanics and Quantum Chemical Calculations, Wavefunction Inc.:Irvine , USA, 2003.
28. Young DC. Computational Chemistry, Wiley: New York, 2001.
29. Rassolov V, Pople JA, Ratner M, Redfern PC, Curtiss LA. 6-31G* basis set for third-row atoms, J. Comp. Chem., **2001,** 22(9), 976-984.
30. Luty T, Ordon P, Eckhardt CL. A model for mechanochemical transformations: Applications to molecular hardness, instabilities, and shock initiation of reaction, J. Chem. Phys., **2002**, 117, 1775- 1785.

NEW FRONT. CHEM. (**2014**)
Volume 23, Number 2, pp. 91-98
ISSN 2393-2171; ISSN-L 2393-2171
© West University of Timişoara

Former: Ann. West Univ. Timisoara – Series Chem.
ISSN: 1224-9513

Article

LEACHING OF BORON FROM A COLEMANITE ORE IN SOME ORGANIC AND MIXED ORGANIC-AQUEOUS SOLVENT SYSTEMS

Lemi Türker[1♣]***, Selçuk Gümüş***[1,2]***, Şahinde Demirci***[1]***, Ceyhan Kayran***[1]

[1] Middle East Technical University, Department of Chemistry, 06531, Ankara, TURKEY
[2] Kimya Bölümü, Yüzüncü Yıl Üniversitesi, 65080, Kampüs, Van, TURKEY

ABSTRACT

In order to leach boron from colemanite ore (from Hisarcık (Kütahya)-Turkey), various organic and mixed organic–aqueous solvent systems have been considered, which are aqueous solutions of glycerol, ethylene glycol, ethanolamine and diethylene glycol in different concentrations. The highest percentage of boron leached has been achieved by water-glycerol system with 1:1 by volume. While 50.5 % of the B_2O_3 in colemanite has been extracted in acidic medium, it is found that the use of very strongly acidic medium is not necessary. Moreover, heating the leaching solution does not increase the percentage of boron leached, either.

Keywords: Leaching of Boron, Azomethine H Method, organic–aqueous solvent systems, glycerol, Colemanite.

1. INTRODUCTION

Colemanite is one of the hydrated boron minerals having the composition of $Ca_2B_6O_{11}\cdot 5H_2O$ (Hydrated Calcium Borate Hydroxide). Others to be mentioned are borax $Na_2B_4O_7.10H_2O$), Boronatrocalcite ($NaCaB_5O_9.8H_2O$), hydroborocalcite ($MgCaB_6O_{11}.6H_2O$)

♣ Correspondent author: Tel:+90 312 2103244, Fax: +90 312 2103200, E-mail: lturker@metu.edu.tr

and pandermite ($Ca_4B_{10}O_{19}.7H_2O$) [1]. Colemanite like other borates, is a complex mineral, that is found in playa lakes and other evaporite deposits. The basic structure of colemanite contains endless chains of interlocking $BO_2(OH)$ triangles and $BO_3(OH)$ tetrahedrons with the calciums, water molecules and extra hydroxides interspersed between the chains.

Turkey has 60 % of the world boron deposits in which its minerals are in the form of hydrated borates containing Ca, Mg, and Na. Colemanite is also found in California and Nevada in USA. In Chile colemanite ores are deposited near Bacos del Toro. Boron ores are used in glass, ceramics, soap, and detergent industries, in metallurgical and nuclear processes, and in the production of various boron compounds used in different industrial areas. Boric acid, borax, boric oxide, and refined hydrated sodium borates and perborates are important boron compounds economically.

Various studies have been carried out to produce boron compounds, especially boric acid and borax from boron ores. The dissolution kinetics of pure and clay-containing colemanite were studied in SO_2-saturated water, and it was found that dissolution processes were chemically controlled for both cases. However, the former had a larger apparent activation energy than the latter [2,3]. In another study (Boncukçuoğlu et al.[4]), the evaluation of the reactor waste in borax production was investigated to recover B_2O_3 and therefore to reduce the toxic effect of the waste. Also, some of these studies include the production borax from colemanite by using NaCl and seawater,[5] boric acid from sulfuric acid and borax [6]. In addition, the dissolution of colemanite and other boron ores has been carried out in various acid solutions [7- 15].

Several complexing agents are commonly used for the spectrophotometric determination of boron in water including curcumin, carmine, and dianthrimide. However, their adaptation to automated procedures is not feasible because either evaporation to dryness or a strong acid medium is required prior to color development.

The condensation product of H acid (8-amino-1-naphthol-3,6-disulfonic acid) and salicylaldehyde, azomethine H, was used by Shanina et al.[16] for the determination of boron in complex borenes and boranes. Basson et al.[17] successfully adapted azomethine H into an automated procedure for the determination of boron in aqueous plant tissue extracts. Basson et al.[18] later incorporated an in situ preparation of azomethine H into the manifold to circumvent the time required for outside preparation of the complexing agent.

The purpose of this study was to adapt the azomethine H procedure for the routine determination of boron, leached from colemanite by a variety of organic solvents (glycerol, ethylene glycol, ethanolamine and diethylene glycol). The azomethine H method worked in a buffered system, is a good alternative to most attractive detection systems, such as, inductively coupled plasma (ICP-OES) spectrometry, with high sensitivity [19].

2. EXPERIMENTAL METHOD

Colemanite ore obtained from Hisarcık (Kütahya)-Turkey has a particle size of 150 μ and it is known to contain 39.4 % B_2O_3. Table 1 displays the composition of the ore.

18.4 ppm boron stock solution has been prepared by dissolving 0.114 g of analytical reagent grade H_3B0_3 in water and diluting to 1 L. A series of standards in the concentration range from 1.84 to 9.22 ppm boron have been prepared by appropriate dilution of the stock with water. The boron stock and standard solutions can also be prepared from $Na_2B_40_7.10H_20$.

The azomethine H solution has been prepared by dissolving 0.45 g of azomethine H and 1.0 g of ascorbic acid in water with gentle heating (50 °C) and stirring and diluting to 100 mL. This temperature is not critical and is used only to hasten dissolution of the reagents.

The buffer solution has been prepared by dissolving 250 g of ammonium acetate ($NH_4C_2H_3O_2$) and 15 g EDTA in a solution containing 400 mL water and 125 mL acetic acid. Ca, Mg and Fe which are present in the ore may interfere when boron is determined directly in samples. It is found that ascorbic acid and EDTA addition to the reaction system can be very effective in masking these ions and greatly improve the selectivity [20].

Table 1: Chemical composition of the colemanite ore used, %.

Composition	%	Composition	%
B_2O_3	39.4286	Fe_2O_3	0.6870
CaO	25.3863	As_2O_3	0.4294
Na_2O	0.3352	SiO	1.6958
MgO	2.4586	TiO_2	0.5078
Al_2O_3	1.2550	K_2O	0.6352
SiO_2	2.8674	BaO	0.0261
SO_3	1.2776	Moisture	0.3743

All chemicals must be analytical grade or better and deionized water has to be used to prepare all the solutions. Optimal results are obtained when the azomethine H solution is prepared fresh.

Boron concentrations were measured in 1.00-cm sample cells, at 420 nm, according to Azomethine H method [21,22] by a Shimadzu double beam UV-VIS spectrophotometer, Model UV 1601.

3. RESULTS AND DISCUSSIONS

It is known from the literature that, boron may be extracted as one of its organic complexes such as (a) the boron-2-ethyl-1,3-hexanediol complex of boron into chloroform or benzene,[23,24] (b) the 2,4-dinitro-1,8-naphthalenediol complex of boron into toluene,[25] or (c) the complex of boron with a 24% solution of 2,4-dimethyl-2,4-octanediol into isopentanol [26].

In the present study, boron has been leached from colemanite, by the application of different aqueous-organic solvent systems, such as, glycerol (**G**), ethylene glycol (**EG**), ethanolamine (**EA**) and diethylene glycol (**DEG**). The determination of the amount of extracted boron has been measured by the application of the azomethine H method, which is reported to give no significant differences with the high cost spectroscopic methods, like ICP-OES spectrometry [27]. The detection limit for the Azomethine-H method has been found to be 1.5 % B_2O_3, the present case.

Presently, three parameters have been considered for the design of the leaching process from colemanite. These are (i) Type of the organic solvent and the solvent/water ratio, (ii) Acidity of the leaching solution, (iii) Temperature of the leaching medium.

(i) The effects of solvent and organic solvent/water ratio on the leaching

At first, the leaching experiments have been performed with aqueous (water only) and organic (glycerol only) solvent systems. The amount of extracted boron has been increased from 15.9 % to 26.6 %, by the use of glycerol as the leaching solvent. However, mixing of the leaching solution was difficult in the case of glycerol, due to its very viscous character. Therefore, aqueous-organic solvent mixture systems were used.

Another important parameter in leaching of boron from colemanite was the organic solvent/water ratio. The achievement of the same leaching of boron with lower organic solvent ratios would be more economic for industrial applications. Therefore, boron leaching experiments have been performed with different water/organic solvent ratios and the results have been reported in Table 2. But unfortunately, lowering the ratio of the organic component in the leaching solution leads to decrease in the percentage of boron leached for all cases.

Table 2: Effect of acidity of the leaching solution on the leaching of boron[a].

	EG	**G**	**EA**	**DEG**
No acid	10.6 ± 0.03	26.6 ± 0.01	4.0 ± 0.02	14.9 ± 0.03
10^{-2} M HCl	20.2 ± 0.02	50.5 ± 0.02	7.3 ± 0.04	23.5 ± 0.01
1.2 M HCl	20.4 ± 0.03	50.9 ± 0.03	7.4 ± 0.03	23.9 ± 0.02

a: Average of five measurements.

Table 3: Effect of aqueous/organic solvent ratio on the percentage of boron leached (at 1 hour mixing)[a].

	% Organic Component			
Organic Solvent	**100**	**50**	**30**	**20**
G	26.6 ± 0.01	50.5 ± 0.03	38.8 ± 0.02	35.2 ± 0.05
DEG	13.4 ± 0.04	23.5 ± 0.04	18.2 ± 0.02	12.3 ± 0.02
EG	16.1 ± 0.02	15.6 ± 0.02	14.4 ± 0.01	12.9 ± 0.01
EA	2.5 ± 0.01	7.3 ± 0.01	3.2 ± 0.02	0.9 ± 0.01

a: Average of five measurements

In the rest of the study, all the experiments have been performed with the aqueous solutions of the organic solvents with 1:1 ratio (see Table 2).

After the achievement of an increase in the percentage of boron leached by glycerol, other alcoholic organic solvents (ethylene glycol, ethanolamine and diethylene glycol) have been considered as the organic component of the leaching solution. Among the four organic solvents considered, maximum and minimum the percentage of boron leached have been observed in the cases of glycerol and ethanolamine, respectively (see Table 3).

(ii) The effect of HCl concentration on the leaching

It is well known from the theoretical literature that leaching performance becomes greater in acidic solutions [3,28]. Therefore, the leaching solutions were acidified with the use of different amounts of concentrated HCl. Acidifying the leaching solution has effectively increased the percentage of boron leached and the amount of leached boron has been increased almost double. However, making the solution more and more acidic than 10^{-2} M, had a very little effect on the amount of leached boron (see Table 2). Figure 1 shows the graph for the amount of B_2O_3 vs. time for the four solvents used at 10^{-2} M HCl concentration.

Figure 1: Effect of the type of the organic solvent on the percentage of boron leached at 10^{-2} M HCl concentration. (2.5 g colemanite is mixed in 50 mL of solution which is 1:1 organic solvent-aqueous mixture).

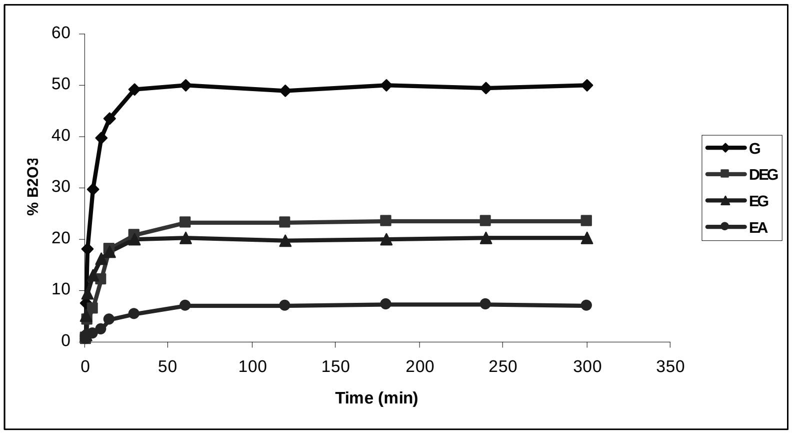

Figure 2: Effect of the type of the organic solvent on the percentage of boron leached at 10^{-2} M HCl concentration (at initial times). (2.5 g colemanite is mixed in 50 mL of solution which is 1:1 organic solvent-aqueous mixture).

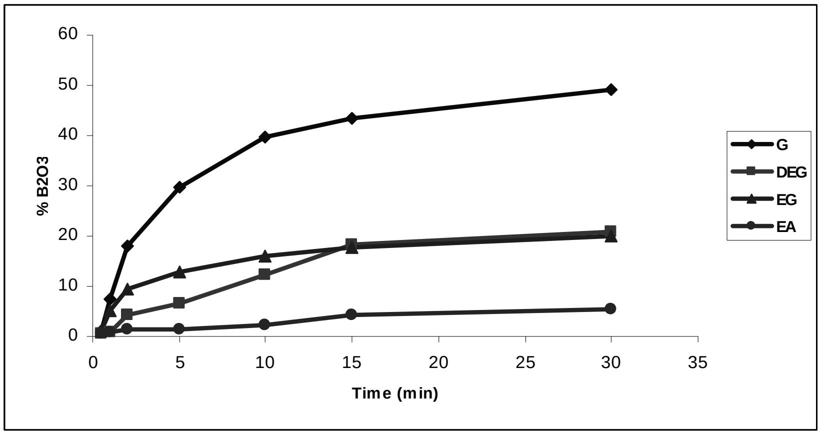

As can be seen from the figure, water-glycerol (in 10^{-2} M HCl) system has been found to be the best among all for the leaching of boron from the colemanite ore samples. Figure 2 shows the change in the amount of B_2O_3 leached at initial times.

(iii) Effect of temperature on the leaching of boron

Increasing the temperature of a solution will lower the intermolecular attraction (hydrogen bonding in this case) between solvent molecules. This may result in lowering the viscosity of the leaching solution and the problems with mixing the leaching solution would be overcome. Thus, the present leaching experiments have been performed at 25 ºC and 60 ºC. The percentage of boron leached at 60 ºC has been found to be slightly higher than that of leaching at 25 ºC.

4. CONCLUSIONS

In the present study, leaching of boron from colemanite ore has been performed with different aqueous-organic solvent systems. The azomethine H method has been used for the determination boron. The detection limit for this method is found to be 1.5 % B_2O_3. The results showed that, glycerol-water system is the best solvent to leach boron from colemanite. The amount of B_2O_3 extracted from colemanite has been reached to 50.5 % with the glycerol-water system while 23.5 %, 15.6 % and 7.3 % leaching has been achieved by the use of **DEG**, **EG** and **EA**, respectively.

It is necessary to perform the leaching process in acidic medium. However, it is found to be unnecessary to use very strongly acidic solutions. The ratio of the aqueous and organic components is important, since the decrease of the percent of the organic solvent decreases the percentage of boron leached and the increase of the percent of the organic solvent increases the cost of leaching process for the industrial applications. The maximum percentage of boron leached has been achieved when the ratio of the organic-aqueous mixture is 1:1 by volume.

During the design of the experiments, the viscosity problem of organic components has been thought to be overcome by heating the leaching solution. But then, it is found that leaching process at higher temperatures is not essential, since the viscosity problem has been solved by mixing the organic solvents with water.

ACKNOWLEDGEMENT

The authors want to thank TUBITAK (Scientific and Technological Research Council of Turkey) (105M347 project) for financial support.

REFERENCES

1. Betekhtin A.; A Course of Mineralogy, Mir Pub. Moscow, **1970**.
2. Kocakerim M.M.; Alkan M. Dissolution kinetics of colemanite in SO_2 saturated water. *Hydrometallurgy* **1988**, *19*, 385-392.

3. Küçük Ö.; Kocakerim M.M., Yartaşı A., Çopur M. Optimization of dissolution of ulexite saturated with sulphur dioxide. *Ind. Eng. Chem. Res.* **2002**, *41*, 2853-2857.
4. Boncukçuoğlu R.; Kocakerim M.M., Erşahan H. Upgrading of the reactor waste obtained during borax production from tincal. *Miner. Eng.* **1999**, *12*, 1275-1280.
5. Lynn L.; *Borax, Ger. Offen.* 2, 337, 506 A1 19740221, *Chem Abs.* **1974**, *81*, 5128e.
6. Dinu G.; Mohai S., Adam I. Boric Acid from Borax. *Rom.* 67, 967, *Chem. Abs.* **1979**, *94*, 194376m.
7. Davies T.W.; Çolak S., Hooper R.M. Boric Acid Production by The Calcination and Leaching of Powdered Colemanite. *Powder Technol.* **1991**, *65*, 433-440.
8. Imamutdinova V.M.; Rate of borate dissolution in acetic acid solutions. *Zh. Prikl. Khim.* **1970**, *43*, 452-5.
9. Kononova G.N.; Nozhko E.S. Nature of the sulfuric acid dissolution of magnesium borates. *Zh. Prikl. Khim.* **1981**, *54*, 397-9.
10. Alkan M. M.; Kocakerim M.M., Çola S. Dissolution kinetics of colemanite in water saturated by carbon dioxide. *J. Chem. Technol. Biotechnol.* **1985**, *35A*, 382-6.
11. Tunç M.; Kocakerim M.M., Gür A., Yartaşı A., A semi-empirical kinetic model for dissolution of ulexite in aqueous acetic acid solutions. *Energy, Educ., Sci. Technol.* **1999**, *3*, 1-10.
12. Tunç M.; Gür A., Kocakerim M.M., Yartaşı A., Dissolution of ulexite in sulphuric acid solutions for high solid-to-liquid ratios. *Energy, Educ., Sci. Technol.* **1999**, *3*, 32-41.
13. Morales G.V., Capretto M.E., Fuentes L.M., Quiraga O.D. Dissolution kinetics of hydroboracite in water saturated with carbon dioxide. *Hydrometallurgy* **2000**, 58, 127-133.
14. Demirbaş A.; Recycling of lithium from borogypsum by leaching with water and leaching kinetics. *Resour., Conserv. Recycl.* **1999**, 25, 125-131.
15. Erdoğan Y.; Aksu A., Demirbaş, Abalı Y. Analyses of boronic ores and sludges and solubilities of boron minerals in CO_2-saturated water. *Resour., Conserv. Recycl.* **1998**, 24, 275-283.
16. Shanina T.M.; Gelman N.E., Mikhailowskaya V.S., Quantitative analysis of organometallic compounds. Spectrophotometric microdetermination of boron. *Fresenius' Zeitschrift fuer Analytische Chemie* **1967**, *22*, 782-7.
17. Basson W.D.; Bohmer R.G., Stanton D.A. An automated procedure for the determination of boron in plant tissue, *Analyst.* **1969**, 34, 1135-1141.
18. Basson W.D.; Pille P.P., Du Preez A.L. Automated in situ preparation of azomethine H and the subsequent determination of boron in aqueous solution. Analyst 1974, 99, 168-170.
19. Evans S.; Krahenbuhl U., Boron analysis in biological material: microwave digestion procedure and determination by different methods. Fresenius J. of Anal. Chem. 1994, 349, 454-549.
20. Saygıdeğer Demir B.; Serindağ O. Determination of boron in grape (Vitis vinifera) by Azomethine H spectrophotometric method Eurasian J. of Anal. Chem. 2006, 1, 1.
21. John M.K.; Chuah H.H., Neufeld J.H., Application of improved Azomethine-H method to the determination of boron in soils and plants. Analytical Letters 1975, 8, 559-568.

22. Wolf B.; Determination of boron in soil extracts, plant materials, composts, manures, water and nutrient solutions. Soil Science and Plant Analysis 1971, 2, 363-374.
23. Agazzi E.J.; Extraction-flame photometric determination of boron. Anal. Chem. 1967, 39, 233-5.
24. Mezger G.;, Grallath E., Stix U., Tolg G., Bestimmung von borspuren in metallen durch emissionsspektrometrie mit ICP-Anregung nach abtrennung als borsäure-ester. Fresenius Z., Anal. Chem. 1984, 317, 765-773.
25. Kuwada K.; Motomizu S., Toei K. Solvent extraction-spectrophotometric determination of boron with 2,4-dinitro-1,8-naphthalenediol and Brilliant Green. Anal. Chem. 1978, 50, 1788-92.
26. Panov V.A.; Semenko K.A., Kuzyakov Y.Y. Extraction-flame molecular emission spectrometric determination of boron with pulsed nebulization of extract. Zhurnal Analiticheskoi Khimii 1989, 44, 1382-7.
27. Şimşek A.; Korkmaz D., Velioğlu Y.S., Ataman O.Y. Determination of boron in hazelnut (Corylus avellana L.) varieties by inductively coupled plasma optical emission spectrometry and spectrophotometry. Food Chem. 2003, 83, 293-296.
28. Türker L. ; Some boric acid esters of glycerol - an ab initio treatment. Ind. J. of Chem. 2006, 45A, 1339-1344.

NEW FRONT. CHEM. (**2014**)
Volume 23, Number 2, pp. 99-110
ISSN 2393-2171; ISSN-L 2393-2171
© West University of Timișoara

Former: Ann. West Univ. Timisoara – Series Chem.
ISSN: 1224-9513

Article

HYDROGEN PEROXIDE PHOTOLYSIS WITH DIFFERENT UV LIGHT SOURCES INCLUDING A NEW UV-LED LIGHT SOURCE

Franco Cataldo (1,2) ♣
[1]Actinium Chemical Research srl, Via Casilina 1626A, Rome 00133, Italy.
[2]Università della Tuscia, Dipartimento di Scienze Ecologiche e Biologiche, Via S. Camillo de Lellis, Viterbo, Italy

ABSTRACT

Hydrogen peroxide 0.1% was photolyzed using 17W low pressure mercury arc lamp and 125 W high pressure mercury arc lamp. The decomposition kinetics was followed through the pseudofirst order kinetics and different conditions of temperature and pH were explored. H_2O_2 0.1% was also photolyzed at 360 nm through a new UV-LED 3W light source using a flow reactor. The kinetics rate constant achieved with the UV-LED photolysis is at least one order of magnitude lower than that achieved with the low pressure mercury arc lamp. Other drawbacks of the UV-LED photolysis were evidenced.

Keywords: Hydrogen peroxide, photolysis, UV-Hg light sources, UV-LED light source.

1. INTRODUCTION

Hydrogen peroxide is considered an environmentally safe reagent since its decomposition leads, in general, to the formation of water and oxygen [1]. The main industrial use of hydrogen peroxide are as oxidizing agent and as disinfectant and sterilant alone or in the form of peracids (e.g. peracetic acid) [1]. Hydrogen peroxide is one of the preferred reagent in wastewater treatment and in the advanced oxidation processes (AOPs) [1].

♣ Correspondent author: Phone/Fax ++39-06-94368230; E-mail: franco.cataldo@fastwebnet

After industrial use, the resulting diluted solutions of H_2O_2 should be decomposed before being disposed. A number of catalysts are known as effective decomposition agents of diluted hydrogen peroxide. The undisputed most effective catalyst is the enzyme catalase which is widespread in nature being present in animals, plants and lower organisms. The most common catalase enzyme used industrially is from bovine liver, having the incredibly high H_2O_2 decomposition rate constant of 3.2×10^5 s^{-1} [2,3]. Another highly selective catalyst capable to decompose H_2O_2 is Pt sol with a rate constant of 7.1×10^2 s^{-1} [2]. According to Jones [1] palladium is even more effective than platinum. Another very important and practical catalyst for diluted H_2O_2 decomposition is MnO_2 which however is several orders of magnitudes slower than catalase. In fact, k values of 1.5×10^{-4} s^{-1} were measured at pH =3 till 9.7×10^{-4} s^{-1} at pH = 10 for the diluted hydrogen peroxide decomposition on manganese dioxide [4,5]. It was also put in evidence that some stabilizer normally added to H_2O_2 like for example pyrophosphates may reduce the catalytic activity of pyrolusite (MnO_2) [6]. Also ferric ions and iron oxide catalyze the decomposition of H_2O_2 and the maximum rate constant reported was 2.7×10^{-3} s^{-1} [7,8].

Other examples of H_2O_2 decomposition catalysts (without the claim of being comprehensive) are iron-cobalt oxides [9], certain rare earth perovskites [10], copper (II) ions [11], water-ceramic interfaces [12]. A special mention should be deserved on the H_2O_2 decomposition on activated carbon with rate constants in the range comprised between 6×10^{-4} and 3×10^{-2} s^{-1} [13,14].

The decomposition of H_2O_2 leads, under certain circumstances, not only to common molecular oxygen but also to the reactive singlet oxygen as underlined in a rather comprehensive work [15]. Therefore care must be taken in the disposal of the generated oxygen.

The main drawbacks in H_2O_2 decomposition using a catalyst like those mentioned above are linked to the necessity to remove the the catalyst once it reaches exhaustion and its substitution. Additionally, some of the mentioned catalyst can leach and release ions into the treated water, so that hydrogen peroxide is destroyed but the resulting water results polluted by undesired transition metals ions. Furthermore, certain catalysts like catalase must be dissolved into hydrogen peroxide to display in full their potential, posing again the problem of catalyst removal from the solution.

An alternative way to decompose diluted H_2O_2 involves the use of a UV light source [16]. The process of H_2O_2 decomposition can be generally described by the simple reaction scheme $H_2O_2 \rightarrow 2 \bullet OH$, but in reality is much more complex and characterized by a quantum yields approximately ≈ 1.0-1.5 in a wide range of wavelengths used for irradiation spanning from 193 nm to the canonical 254 nm to the UV-A represented by 308 and 354 nm [16-27]. Special variants in the photolysis of H_2O_2 involve the photocatalytic decomposition process where the UV irradiation is conducted in presence of a suspension of titanium dioxide [23], or the use of highly energetic vacuum UV radiation [24].

This paper is dedicated to a comparison of different UV light sources in the decomposition of diluted H_2O_2.

2. EXPERIMENTAL

2.1. Materials and Equipment

Hydrogen peroxide 35% was supplied from Evonik. Sulfuric acid, potassium iodide and ammonium molybdate were obtained from Sigma-Aldrich.

For the UV irradiations use was made of 17W low pressure mercury lamp from Helios Italquartz having an almost monochromatic emission at 254 nm. The lamp was inserted into a cylindrical quartz sheath having a length 18 cm. The sheath was then inserted into a Durhan glass reactor filled with 200 nm of diluted H_2O_2.

The UV irradiation with a medium pressure mercury lamp was performed with 125 W lamp with water jacketed quartz sheath (18 cm length) and dedicated glass reactor. Also this lamp was from Helios Italquartz with main emissions at 365 nm and in the visible, with minor lines at 222-265 nm. For a detailed description of the photochemical apparatus used and the mercury lamp main emission see ref. [28].

The UV-LED irradiation was performed using 3W LED (=light emitting diode) with main emission at 360 nm. The led was characterized by a Shimadzu UV 1670 spectrophotometer and as shown in Fig.1 the diode main emission occurs as a monochromatic line at about 360 nm, in the UV-A region. However, this line is accompanied by a broader and intense emission at 204 nm (in the UV-C region) which has saturated the spectrophotometer detector. It is not sure if the line at 204 nm is due to an artifact since the current UV-LED lamps are known to irradiate only at about 360 nm.

Figure 1: Emission lines from the light emitting diode as recorded in the UV-VIS spectrometer. The main emission is located at 359 nm as a narrow line. However, there is also another emission at 204 nm which appears even more intense (the signal is saturated) and broader than the emission at 359 nm. The emission above 750 nm is near infrared emission and goes beyond 800 nm

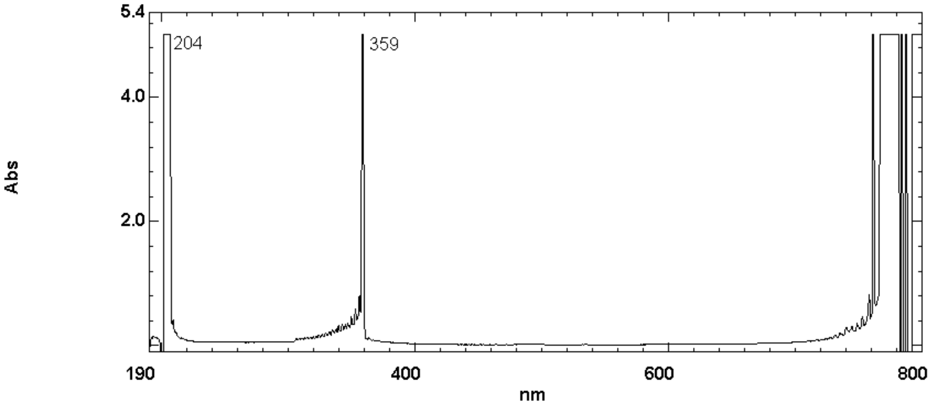

Fig. 2 shows the home-made UV-LED reactor made in polycarbonate and with the light source mounted at the top. The diluted hydrogen peroxide solution was circulated into the reactor using an external peristaltic pump.

Figure 2: UV-LED reactor. The lamp is at the top of the reactor and the H_2O_2 solution is circulated through the reactor with inlet at the bottom and outlet at the top

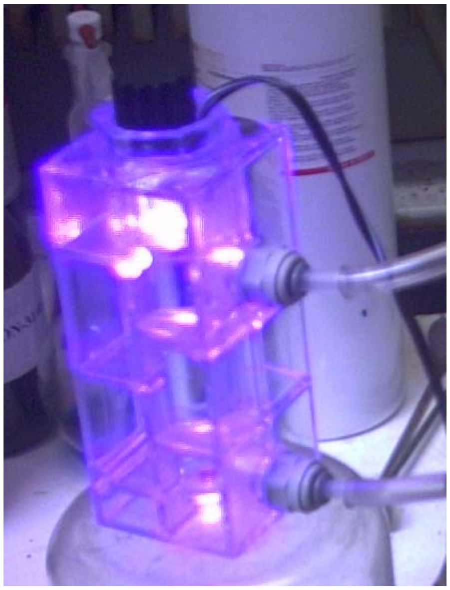

2.2. Experimental Method/Model

Stock solutions of approximately 0.1% H_2O_2 were prepared by sampling 1.5 ml of H_2O_2 35% and diluting with distilled water to a final volume of 500 ml.

The hydrogen peroxide concentration was determined iodometrically following the method of Kolthoff et al. [29]. The method consists in the addition of 1 g of KI to 25 ml of diluted hydrogen peroxide solution followed by the addition of 10 ml of H_2SO_4 2M and 3-4 drops of a solution of ammonium molybdate as catalyst to accelerate the reaction between KI and H_2O_2. The free iodine liberated is titrated with a 0.05 M solution of $Na_2S_2O_3$.

3. RESULTS AND DISCUSSIONS

3.1 GENERAL ASPECTS OF THE H_2O_2 DECOMPOSITION REACTION

The thermodynamics parameters of H_2O_2 decomposition according to the general reaction:

$$2\ H_2O_2 + h\nu \rightarrow [4\ \bullet OH] \rightarrow 2\ H_2O + O_2 \qquad (1)$$

are all favorable. In fact the Gibb's free energy of reaction (1) is largely negative underlining that the reaction is thermodynamically allowed: ΔG_R = -237 kJ/mol. The enthalpy of reaction (1) is also negative ΔH_R = -190 kJ/mol, showing that the decomposition reaction occurs exothermally.

From the photochemical standpoint, as discussed in the introduction, the quantum yield of reaction (1) Φ = 1.0-1.5 Einstein in a wide range of wavelengths. More precisely, it was reported that the H_2O_2 photolysis is effective at any wavelength <380 nm, where H_2O_2 starts to absorb appreciably light [30]. Such quantum yield values around the unity clearly suggest that chain reactions are hindered by an effective termination processes of the •OH and •OOH radicals.

A general description of the main reactions occurring in the photolysis of H_2O_2 were reported as follows [31]:

Light absorption initiation

$$H_2O_2 + h\nu \rightarrow 2\ \bullet OH \qquad k_1 = \Phi\ I_p \tag{2}$$

propagation

$$\bullet OH + H_2O_2/\ HO_2^- \rightarrow \bullet OOH/\ O_2^- + H_2O \quad k_2 = 2.7x10^7 \text{ to } 7.5x10^9x10^{pH-11.8}\ M^{-1}\ s^{-1} \tag{3}$$

$$\bullet OOH + H_2O_2 \rightarrow H_2O + \bullet OH + O_2 \qquad k_3 = 3.7\ M^{-1}\ s^{-1} \tag{4}$$

termination

$$2\ \bullet OOH \rightarrow H_2O_2 + O_2 \qquad k_4 = 8.3x10^{-5}\ M^{-1}\ s^{-1} \tag{5}$$

In addition, the disproportionation reaction of of $\bullet OOH + O_2^{\bullet -}$ is expected to contribute to H_2O regeneration as shown below:

$$\bullet OOH + O_2^{\bullet -} + H_2O \rightarrow H_2O_2 + O_2 + OH^- \qquad k_5 = 9.7x10^7\ M^{-1}\ s^{-1} \tag{6}$$

The above reactions suggest that under determined conditions the photolysis of H_2O_2 could be completely compensated by the termination and disproportionation reactions which are able re-generate hydrogen peroxide.

3.2 Photolysis of H_2O_2 by low pressure and high pressure mercury lamps

The kinetics of H_2O_2 decomposition is described by a second order kinetics law [31]. However, in first approximation, the use of pseudofirst order kinetics is sufficient to describe the concentration decay of hydrogen peroxide as function of the irradiation time [32], considering also that this study was made on diluted ≈0.1% H_2O_2, a concentration which is closer to the real applied conditions . Consequently, the simple equation:

$$\ln\{[H_2O_2]_t/[H_2O_2]_0\} = kt \tag{7}$$

was used in the determination of the kinetic rate constant k (expressed in s^{-1}) represented by the slope of the experimental data linking the first member of equation 7 with t, the irradiation time in seconds [2,32]. Fig.2 shows an example of this evaluation of the experimental data in the photolysis of 0.1% H_2O_2 in presence of Fe^{3+} ions with a low pressure and a medium-high pressure mercury lamp. Fe^{3+} ions were added $5x10^{-3}$ M were added in the intention to depress the termination reaction (5) as well as the disproportionation reaction (6). The pseudofirst kinetics rate constants determined from the graph in Fig. 3 show that the low pressure mercury lamp, although less powerful in light intensity (17 W) gives a higher rate constant for the decomposition of H_2O_2 with $k_{lowP} = -4.57x10^{-4}\ s^{-1}$ against the high pressure mercury lamp working at 125 W with $k_{hiP} = -3.74x10^{-4}\ s^{-1}$.

Figure 3: Pseudofirst order kinetics in the photolysis of 0.1% H_2O_2 with a low pressure mercury lamp (blue diamonds) and with a high pressure mercury lamp (red squares)

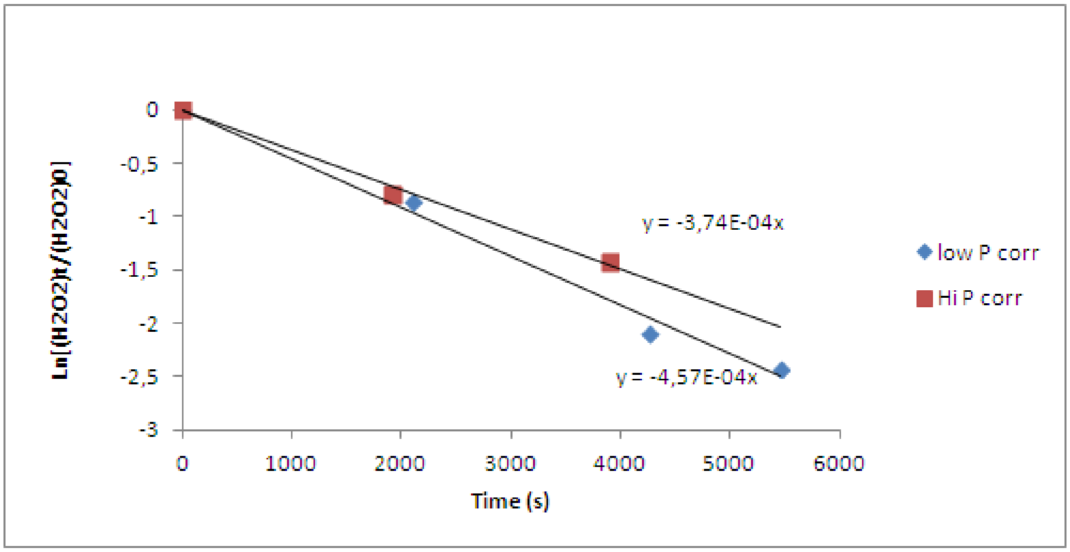

The reason why the low pressure mercury lamp is giving similar photolytic results as the high pressure mercury lamp (although it works at lower power than the high pressure lamp) is due to the fact that all the 17W power is released at 254 nm where H_2O_2 has a molar extinction coefficient of 19.6 L $mol^{-1}\ s^{-1}$. Instead, at longer wavelengths, where large part of the irradiation power of a high pressure mercury lamp is released the molar extinction coefficient of H_2O_2 is much lower: e.g. at 300 nm $\varepsilon = 1$ L $mol^{-1}\ s^{-1}$, at 320 nm $\varepsilon = 0.22$ L $mol^{-1}\ s^{-1}$, at 340 nm $\varepsilon = 0.047$ L $mol^{-1}\ s^{-1}$, and at 360 nm $\varepsilon = 0.01$ L $mol^{-1}\ s^{-1}$. Thus, with a low pressure mercury lamp, the lower power (17 W) is released exclusively as photons at 254 nm where H_2O_2 has the highest light absorption cross section (in the spectral range considered here). On the other hand the high power of the high pressure mercury lamp (125 W) is dispersed in a wider range of wavelengths including also wavelengths where the absorption cross section of H_2O_2 is negligible and hence is lost without any effect.

In Table 1 are summarized the results of a series of photolysis experiments made on 0.1% hydrogen peroxide and evaluated through the pseudofirst order kinetic law. The data show that the addition of Fe^{3+} ions to 0.1% H_2O_2 does not lead to any decisive improvements in the photolysis rate constants:

$k_{lowP} = -4.57x10^{-4}\ s^{-1}$ with Fe^{3+}
against
$k_{lowP} = -4.8x10^{-4}\ s^{-1}$ without Fe^{3+}
and
$k_{hiP} = -3.74x10^{-4}\ s^{-1}$ with Fe^{3+}

against
$k_{hiP} = -5.1x10^{-4}\ s^{-1}$ without Fe^{3+}.

Contrary to the expectation, the data show an inhibitory effect of the Fe^{3+} ions in the photolysis of 1% H_2O_2. In the absence of Fe^{3+} ions the photolysis rate constants of the two mercury lamps are practically the same: $k_{lowP} = -4.8x10^{-4}\ s^{-1}$ against $k_{hiP} = -5.1x10^{-4}\ s^{-1}$.

Table 1 shows also the temperature effect and the pH effects in the photolysis of H_2O_2. It is well known that the photochemical reactions are not sensitive to the change of temperature since the mechanism of activation is not affecting the translational kinetic energy of molecules but only and selectively their electronic state. Therefore, it is not a surprise to see that $k_{lowP} = -4.8x10^{-4}\ s^{-1}$ at 20°C against $k_{lowP} = -5.5x10^{-4}\ s^{-1}$ at 45°C. For thermally activated reactions it is valid the Arrhenius law which states as general rule of thumb that any reaction rate double by the increase of 10°C in temperature. Thus for thermally activated reactions we must see an increase in the reaction rate by an order of magnitude. Instead in the photochemical reaction under study there was no significant increase in the decomposition rate constant by passing from 20°C to 45°C.

Table 1 shows also the effect of a pH increase from 7 to 10.5-11.0 (at 45°C). The photolysis in alkaline pH conditions causes a significant enhancement of the photolysis rate constant with the low pressure mercury lamp passing from $k_{lowP} = -5.5x10^{-4}\ s^{-1}$ at neutral pH to $k_{lowP} = -1.3x10^{-3}\ s^{-1}$ at pH = 11: one order of magnitude faster. This behaviou was expected by the eq. 3 where an increase in the pH leads to an increase in the propagation rate constant step 3.

Another aspect illustrated in Table 1 is the volume effect. The same 17W lamp was used to irradiate 0.1% H_2O_2 in different volumes 2100 ml, 200 ml and 150 ml. Of course the measured rate constant are linked to the irradiated volume: $k_{2100\ ml} = -4.9x10^{-5}\ s^{-1}$ to normalize such rate constant to a volume of 200 ml the correction factor of 2100/200 = 10.5 should be applied so that $10.5x-4.9x10^{-5}\ s^{-1} = -5.1x10^{-4}\ s^{-1}$ which is almost coincident with the experimental value $k_{200\ ml} = -4.8x10^{-4}\ s^{-1}$. Similarly, to normalize the k value measured on 150 ml which was $k_{200\ ml} = -6.4x10^{-4}\ s^{-1}$, the correction factor 150/200 = 0.75 should be applied to get $0.75x-6.4x10^{-4}\ s^{-1} = 4.8x10^{-4}\ s^{-1}$ which is exactly coincident with the experimental value $k_{200\ ml} = -4.8x10^{-4}\ s^{-1}$.

3.3 Photolysis of H_2O_2 by UV-LED reactor

UV-LED lamps are a great novelty in photochemistry. The limitation of the UV-LED sources at present are linked to the relatively low power emitted by each lamp (3W) and by the fact that the main emission of the UV-LED lamp occurs at about 360 nm (see Fig.1), in the UV-A spectral range which is photochemically less useful than the eventual emission in the UV-B and UV-C spectral range. Despite these limitations, we have used a UV-LED lamp (see Fig. 2) in the photolysis of 1% H_2O_2 in comparison to the photolysis with the traditional low pressure and high pressure mercury arc lamps.

The photolysis data are reported in Table 1 and refer to a volume of irradiated solution of 55 ml which is the capacity of the home-made reactor. From the data collected it is evident that the photolysis rate constant of H_2O_2 with the UV-LED lamp is at least one order of magnitude lower than that measured with the traditional mercury arc lamps. However, for a more straight comparison of the experimental results, the kinetics values reported in Table 1 and referred to a volume of 55 ml of solution should be normalized to a standard volume of 200 ml. Hence the volume correction factor is 55/200 = 0.275 and this gives $k_{UV\text{-}LED200ml}$ = 0.275x-1.5x10^{-5} = -4.1x10^{-6} s^{-1} or $k_{UV\text{-}LED200ml}$ = 0.275x-3.6x10^{-5} = -9.9x10^{-6} s^{-1}. Thus, the UV-LED lamp leads to a 200 ml normalized photolysis rate constant two orders of magnitude lower than that achieved by the traditional mercury arc lamps. The reason of such lower performance of the UV-LED lamp is certainly ascribable not only to the low power of the lamp, but also to the emission in the UV-C where the molar extinction coefficient of H_2O_2 is very low.

Table 1: Summary Of The Photolysis Data On H_2O_2 0.028-0.030 M

Entry #	Process	H_2O_2 (ml)	pH	T(°C)	k (s-1)
1	**UV 17W (Low P Hg)**	200	7	20	-4.8x10^{-4}
2	**UV 17W (Low P Hg)**	200	7	**45**	-5.5x10^{-4}
3	**UV 17W (Low P Hg)**	200	10.5	**45**	-1.2x10^{-3}
4	**UV 17W (Low P Hg)**	200	11	**45**	-1.3x10^{-3}
5	**UV 17W (Low P Hg)**	2100	7	20	-4.9x10^{-5}
1	**UV 17W (Low P Hg)**	200	7	20	-4.8x10^{-4}
6	**UV 17W (Low P Hg)**	150	7	20	-6.4x10^{-4}
7	**UV 125W (High P Hg)**	200	7	20	-5.1x10^{-4}
8	**UV 17W (Low P Hg) + Fe^{3+}**	200	8	20	-4.6x10^{-4}
9	**UV 125W (High P Hg) + Fe^{3+}**	200	8	20	-3.7x10^{-4}
10	**UV-LED 360 nm**	55	7	20	-1.5x10^{-5}
11	**UV-LED 360 nm**	55	7	20	-3.6x10^{-5}
12	**UV-LED 360 nm**	55	11.5	20	-6.8x10^{-5}

Taking the $k_{UV\text{-}LED200ml}$ = -9.9x10^{-6} s^{-1} as our reference and multiplying that rate constant by 6 UV-LED lamps (3 W each) put in series the new $k'_{UV\text{-}LED200ml}$ = 6x 9.9x10^{-6} = 5.9x10^{-5} s^{-1}. This calculation shows that even operating with 18 W of UV-LED lamps the H2O2 photolysis rate constant will be one order of magnitude lower than that achieved using 17W of a low pressure mercury arc lamp.

The photolysis of 0.1% H_2O_2 with any mercury arc lamp proceeds straightforward till the complete disappearance of the peroxide. A curious and quite unexpected phenomenon was observed in the case of the UV-LED photolysis of 0.1% H_2O_2 as shown in Fig. 4. At the beginning the H_2O_2 photolysis proceeds following strictly the pseudofirst order kinetic law with the k values reported at the bottom of Table 1. However, prolonged photolysis does not lead to the complete decomposition of H_2O_2 but instead leads to the prevalence of the opposite reaction, i.e. formation and accumulation of H_2O_2. The exact reason of this inversion of trend is not fully clear but based on the equations 2-6, it is evident that once reached a minimal critical concentration of H_2O_2 the photolysis and propagation reactions (2-4) are overcome by the termination and disproportionation reactions (5-6) which instead produce H_2O_2 rather than destroying it.

Figure 4: UV-LED photolysis of 0.1% H_2O_2: initially the decomposition of hydrogen peroxide is the prevalent reaction, but after a certain photolysis time the reverse reaction appears to be prevalent and the initial concentration of hydrogen peroxide is recovered and even overcome

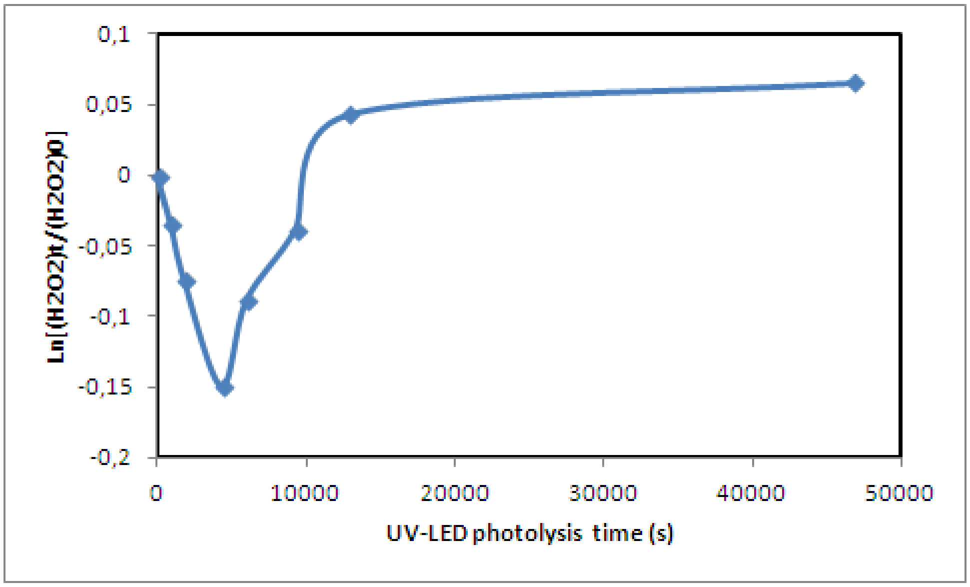

4. CONCLUSIONS

The UV photolysis of 0.1% H_2O_2 was studied under various conditions using three different UV light sources. Traditional mercury arc lamps were used. Low and high pressure mercury arc lamps give almost the same photolysis rate constants although the low pressure mercury lamp was a 17 W lamp while the high pressure mercury lamp was a 125W lamp. The reason of the similar performance resides in the fact that the low pressure mercury lamp emits at 254 nm where H_2O_2 has a high molar extinction coefficient so that all photons emitted by the lamp were used in the photolysis. Conversely the high pressure 125 W lamp emits in a wide ranges of wavelengths and only a fraction of the 125 W energy emitted is used in the photolysis of H_2O_2, for example the light fraction emitted in the UV-A and UV-B spectral range.

The UV photolysis of H_2O_2 is not sensitive to temperature changes, as expected, while instead the phoolysis is considerably enhanced if it is conducted in alkaline H_2O_2 for example at pH = 11. The addition of Fe^{3+} ions which were expected to enhance photochemical yield did not give any improvement to the photolysis rate constant.

The UV photolysis of H_2O_2 was also performed in a new home-made photochemical reactor using a UV-LED diode emitting at 360 nm with a power of 3W. The photolysis rate constant was found two roders of magnitude lower than that achieved with the traditional mercury arc lamps and calculations show that even by working at 18W, the UV-LED photolysis of H_2O_2 is at least one order of magnitude slower than the photolysis performed with 17 W low pressure mercury lamp.

Another drawback of the UV-LED photolysis of H_2O_2 regards the fact that it does not proceed straightforwardly to the complete decomposition of H_2O_2 as in the case of the irradiation with mercury arc lamps. Instead, once reached a minimal concentration the termination and disporportionation reactions overcome the photolysis and the propagation reactions so that H_2O_2 starts to re-accumulate again. Thus, the complete removal of H_2O_2 cannot be achieved with UV-LED photolysis as instead can be achieved with mercury arc lamp photolysis.

REFERENCES

1. Jones, C. *Application of Hydrogen Peroxide and Derivatives*. Royal Soc. Chemistry, Cambridge, 1999.
2. Yeremin, E.N. *The Foundation of Chemical Kinetics*. Mir Publishers, Moscow, 1979. p. 351
3. Keilin, D., Hartree, E. F. (1938). On the mechanism of the decomposition of hydrogen peroxide by catalase. *Proceedings of the Royal Society of London. Series B, Biological Sciences*, *124* (837), 397-405.
4. Hasan, M. A., Zaki, M. I., Pasupulety, L., Kumari, K. (1999). Promotion of the hydrogen peroxide decomposition activity of manganese oxide catalysts. *Applied Catalysis A: General*, *181*(1), 171-179.
5. Do, S. H., Batchelor, B., Lee, H. K., & Kong, S. H. (2009). Hydrogen peroxide decomposition on manganese oxide (pyrolusite): kinetics, intermediates, and mechanism. *Chemosphere*, *75*(1), 8-12.
6. Pirault-Roy, L., Kappenstein, C., Gué, M., rin, Eloirdi, R., & Pillet, N. (2002). Hydrogen peroxide decomposition on various supported catalysts effect of stabilizers. *Journal of Propulsion and Power*, *18*(6), 1235-1241.
7. Lin, S. S., & Gurol, M. D. (1998). Catalytic decomposition of hydrogen peroxide on iron oxide: kinetics, mechanism, and implications. *Environmental Science & Technology*, *32*(10), 1417-1423.
8. De Laat, J., & Gallard, H. (1999). Catalytic decomposition of hydrogen peroxide by Fe (III) in homogeneous aqueous solution: mechanism and kinetic modeling. *Environmental Science & Technology*, *33*(16), 2726-2732.
9. Goldstein, J. R., & Tseung, A. C. C. (1974). The kinetics of hydrogen peroxide decomposition catalyzed by cobalt-iron oxides. *Journal of Catalysis*, *32*(3), 452-465.

10. Lee, Y. N., Lago, R. M., Fierro, J. L. G., & González, J. (2001). Hydrogen peroxide decomposition over $Ln_{1-x}A_xMnO_3$ (Ln= La or Nd and A= K or Sr) perovskites. *Applied Catalysis A: General*, *215*(1), 245-256.
11. Luo, Y., Kustin, K., & Epstein, I. R. (1988). Systematic design of chemical oscillators. 44. Kinetics and mechanism of hydrogen peroxide decomposition catalyzed by copper (II) in alkaline solution. *Inorganic Chemistry*, *27*(14), 2489-2496.
12. Hiroki, A., & LaVerne, J. A. (2005). Decomposition of hydrogen peroxide at water-ceramic oxide interfaces. *The Journal of Physical Chemistry B*, *109*(8), 3364-3370.
13. Khalil, L. B., Girgis, B. S., & Tawfik, T. A. M. (2001). Decomposition of H_2O_2 on activated carbon obtained from olive stones. *Journal of Chemical Technology and Biotechnology*, *76*(11), 1132-1140.
14. Rey, A., Zazo, J. A., Casas, J. A., Bahamonde, A., & Rodriguez, J. J. (2011). Influence of the structural and surface characteristics of activated carbon on the catalytic decomposition of hydrogen peroxide. *Applied Catalysis A: General*,*402*(1), 146-155.
15. Aubry, J. M. (1985). Search for singlet oxygen in the decomposition of hydrogen peroxide by mineral compounds in aqueous solutions. *Journal of the American Chemical Society*, *107*(21), 5844-5849.
16. Baxendale, J. H., & Wilson, J. A. (1957). The photolysis of hydrogen peroxide at high light intensities. *Trans. Faraday Soc.*, *53*, 344-356.
17. Lea, D. E. (1949). The termination reaction in the photolysis of hydrogen peroxide in dilute aqueous solutions. *Trans. Faraday Soc.*, *45*, 81-85.
18. Sauer Jr, M. C., Brown, W. G., & Hart, E. J. (1984). Oxygen (^3P) atom formation by the photolysis of hydrogen peroxide in alkaline aqueous solutions.*The Journal of Physical Chemistry*, *88*(7), 1398-1400.
19. Zellner, R., Exner, M., & Herrmann, H. (1990). Absolute OH quantum yields in the laser photolysis of nitrate, nitrite and dissolved H2O2 at 308 and 351 nm in the temperature range 278–353 K. *Journal of Atmospheric Chemistry*, *10*(4), 411-425.
20. Schiffman, A., Nelson Jr, D. D., & Nesbitt, D. J. (1993). Quantum yields for OH production from 193 and 248 nm photolysis of HNO3 and H2O2. *The Journal of chemical physics*, *98*(9), 6935-6946.
21. Chu, L., & Anastasio, C. (2005). Formation of hydroxyl radical from the photolysis of frozen hydrogen peroxide. *The Journal of Physical Chemistry A*,*109*(28), 6264-6271.
22. Goldstein, S., Aschengrau, D., Diamant, Y., & Rabani, J. (2007). Photolysis of aqueous H_2O_2: quantum yield and applications for polychromatic UV actinometry in photoreactors. *Environmental science & technology*, *41*(21), 7486-7490.
23. Ilisz, I., Föglein, K., & Dombi, A. (1998). The photochemical behavior of hydrogen peroxide in near UV-irradiated aqueous TiO_2 suspensions. *Journal of Molecular Catalysis A: Chemical*, *135*(1), 55-61.
24. Stief, L. J., & DeCarlo, V. J. (1969). Vacuum‐Ultraviolet Photochemistry. IX. Primary and Chain Processes in the Photolysis of Hydrogen Peroxide. The Journal of Chemical Physics, 50(3), 1234-1240.

25. Staehelin, J., & Hoigne, J. (1982). Decomposition of ozone in water: rate of initiation by hydroxide ions and hydrogen peroxide. *Environmental Science & Technology*, *16*(10), 676-681.
26. Glaze, W. H., Kang, J. W., & Chapin, D. H. (1987). The chemistry of water treatment processes involving ozone, hydrogen peroxide and ultraviolet radiation. *Ozone Science and Engineering*, 9, 335-352.
27. Weiss, J. (1952). The free radical mechanism in the reactions of hydrogen peroxide. *Adv. Catal.* 4, 343-365.
28. Ninomiya, I., Naito, T. *Photochemical Synthesis*, Chapter 10, Academic Press, London, 1989.
29. Kolthoff, I.M., Sandell, E.B., Meehan, E.L., Bruckenstein, S. *Quantitative Chemical Analysis*, Chapter 44, Macmillan Company, London, 1973.
30. Lunak, S., Sedlak, P. (1992). Photoinitiated reactions of hydrogen peroxide in liquid phase. *J. Photochem. Photobiol. A Chem.* 68, 1-33.
31. Liao, C.H., Gurol, M.D. (1995). Chemical oxidation by photolytic decomposition of H_2O_2. *Environ. Sci. Technol.* 29, 3007-3014.
32. Petrucci, R.H., Herring, F.G., Madura, J.D., Bissonnette, C. *General Chemistry: Principles and Modern Applications.* 10th edition. Pearson Education Canada Inc. 2011. Chapter 14.

NEW FRONT. CHEM. (**2014**)
Volume 23, Number 2, pp. 111-122
ISSN 2393-2171; ISSN-L 2393-2171
© West University of Timişoara

Former: Ann. West Univ. Timisoara – Series Chem.
ISSN: 1224-9513

Article

THEORETICAL STUDY OF BI-METALLIC Ag_mAu_n;(m+n=2-8) NANO ALLOY CLUSTERS IN TERMS OF DFT BASED DESCRIPTORS

Prabhat Ranjan [1], ***Srujana Venigalla*** [2], ***Ajay Kumar*** [3],
Tanmoy Chakraborty [4♣]

[1,3] Department of Mechatronics; [2,4] Department of Chemistry, Manipal University Jaipur, Dehmi Kalan, Jaipur-303007, India

ABSTRACT

Due to wide applications of bi-metallic nano alloys, the theoretical study of the same is an active field of research. A deep theoretical insight can explore vividly the physico-chemical properties of such compounds. Recently Ag-Au nano alloys have gained a considerable interest for possessing unique engineering properties. In this report, Ag_mAu_n (m + n= 2-8) clusters have been studied invoking DFT based descriptors. Our computed data distinctly exhibits odd-even oscillation behaviour. A successful correlation has been made between computed descriptors and their experimental counterpart. This theoretical analysis is probably the first attempt in this domain.

Keywords: Density Functional Theory, Bi-metallic Nano Alloy, Opto-electronic property.

1. INTRODUCTION

In the recent decades, nanomaterials have deeply integrated into our everyday's life. Since last few years, nanomaterials and nanotechnology have emerged as important research domains of science and technology [1]. The classification of nanoparticles is done in terms of

---

[♣] Correspondent author: Dr. Tanmoy Chakraborty, Tel:0141-3999-100, Extn.: 274, Fax:,
E-mails: tanmoy.chakraborty@jaipur.manipal.edu; tanmoychem@gmail.com

size range of 1-100 nm. That particular size range exists between the levels of atomic / molecular and bulk material [1-5]. Due to existence of a large number of quantum mechanical and electronic effects, nanoparticles possess various unique physico-chemical properties [2-4]. But, there are still some instances of nonlinear transition of certain physical properties, which may vary depending on their size, shape and composition [6, 7]. A large number of scientific reports are available for describing the effects of size and structure to change the optical, electronic, magnetic, chemical and other physical properties of nanoparticles [1, 3, 4]. A deep insight into the research of nanoparticles with well –defined size and structure may lead to some other alternatives for better performance [8]. The nanoparticles, due to its vast applications in the areas of biological labeling, photochemistry, catalysis, information storage, magnetic device, optics, sensors, photonics, optoelectronics, nanoelectronics etc. have got immense importance [1, 3, 9-11].

The noble metals can be extensively applied in several technological areas due to its superior catalytic, magnetic and electronic properties [12–18]. A number of reports are available for describing the conjoint effect of two or more noble metals to enhance the above mentioned properties [13, 19-20]. Now a days, different compositions of nano alloys are being utilized for advancement of methodologies and characterization techniques [21, 13, 19]. A deep study of core-shell structure of nano compounds is very much popular as because its properties can be tuned through the proper control of other structural and chemical parameters. Group 11 metal (Cu, Ag and Au) clusters exhibit the filled inner d orbitals with having one unpaired electron in the valence s shell [22]. This electronic arrangement is responsible to reproduce the exactly similar shell effects [23-27] which are experimentally observed for the alkali metal clusters [28-30]. As a result, bimetallic noble metal clusters follow to exhibit similar physico-chemical trends with bimetallic alkali metal clusters [31-35]. Among the nano clusters of Group 11 elements, the compound formed between Ag-Au is very much popular due to its large scale applications. Fabbi et al. already reported the importance of Ag-Au dimer using dispersed fluorescence spectroscopy [36]. A number of theoretical observations have been made to explore the physico-chemical properties and importance of Ag-Au dimer [37,38]. The location of sliver has a controlling effect on the optical properties of such particles as because optical properties are governed by plasmon resonance frequency of silver, which is also dependent on its structural environment [39]. It has been already established that gold-silver bi-metallic nano clusters, as catalysts can enhance the reaction efficiency and selectivity [40, 41]. Though, a number of experimental studies have been done on this particular type of compounds, a theoretical analysis invoking Density Functional Theory (DFT) is still unexplored.

DFT is one of the most successful techniques of quantum mechanics to explore the electronic properties of materials in terms of quantitative descriptors. As for the larger systems electron density is more manageable as compared to wave function, DFT is very much popular to study the many- body systems [8]. Super conductivity of metal based alloys [42], magnetic properties of nano alloy clusters [43, 44] quantum fluid dynamics [45], molecular dynamics [46], nuclear physics [47, 48] can be extensively studied by DFT methodology. Recently we have established the importance of DFT based descriptors in the domain of drug designing and engineering materials [49, 50, 51, 52].

The study of density functional theory is broadly classified into three sub categories viz. theoretical, conceptual, and computational [53-56]. The conceptual density functional theory is highlighted following Parr's dictum "Accurate calculation is not synonymous with useful interpretation. To calculate a molecule is not to understand it" [57].

In this venture, we have studied bi-metallic Ag-Au nano-clusters in terms of DFT based conceptual descriptors. An attempt has been made to correlate the computed descriptors of the compounds with their experimental counterparts.

2. COMPUTATIONAL METHOD

In this study, we have made a computational analysis on the bi-metallic Nano Alloy clusters of Ag_mAu_n; where m + n =2-8. 3d modeling and structural optimization of all the compounds have been performed using Gaussian 03 [58] within Density Functional Theory framework. For optimization purpose, the Hybrid functional Becke, three parameter, Lee-Yang-Parr (B3LYP) exchange correlation with basis set LanL2dz has been adopted. Energy minimization has been performed without imposing any restriction on molecular spin. We have considered Z-axis as spin polarization axis. In this process, the Symmetrized Fragment Orbitals (SFOs) are combined with auxiliary Core Functions (CFs) to ensure orthogonalization on the (frozen) Core Orbitals (COs).

Invoking Koopmans' approximation [59], we have calculated ionization energy (I) and electron affinity (A) of all the nano alloys using the following ansatz-

$$I = -\varepsilon_{HOMO} \tag{1}$$

$$A = -\varepsilon_{LUMO} \tag{2}$$

Thereafter, using I and A, the conceptual DFT based descriptors viz. electronegativity (χ), global hardness (η), molecular softness (S) and electrophilicity index (ω) have been computed. The equations used for such calculations are as follows:

$$\chi = -\mu = \frac{I + A}{2} \tag{3}$$

$$\eta = \frac{I - A}{2} \tag{4}$$

$$S = \frac{1}{2\eta} \tag{5}$$

$$\omega = \frac{\mu^2}{2\eta} \tag{6}$$

where, μ represents the chemical potential of the system.

3. APPLICATION

In this study, we have made a detail theoretical analysis of Ag-Au bi-metallic Nano clusters in terms of electronic structure theory.

3.1. Results

The orbital energies in form of HOMO (Highest Occupied Molecular Orbital)-LUMO (Lowest Unoccupied Molecular Orbital) gap along with computed DFT based descriptors viz. molecular electronegativity, global hardness, global softness, global electrophilicity index and dipole moment of instant compounds have been reported in the Table-1.

Table 1: Computed DFT based descriptors of Ag_mAu_n; m+n=2-8 nano alloy clusters

Species	HOMO-LUMO Gap (eV)	Electronegativity (eV)	Hardness (eV)	Softness (eV)	Electrophilicity Index (eV)	Dipole Moment (Debye)
AgAu	3.1239	4.7553	1.5619	0.3201	2.3776	2.8191
$AgAu_2$	1.3003	6.0589	0.6501	0.7690	3.0294	0.0000
$AgAU_3$	2.5487	5.4973	1.2743	0.3923	2.7486	2.9422
$AgAu_4$	1.5055	5.3428	0.7527	0.6642	2.6714	0.0000
$AgAu_5$	2.7133	4.6948	1.3566	0.3685	2.3474	0.8952
$AgAu_6$	1.0688	4.8161	0.5344	0.9356	2.4080	0.0000
$AgAu_7$	1.8568	4.8784	0.9284	0.5385	2.4392	3.1101
Ag_2Au	1.4149	3.8366	0.7074	0.7067	1.9183	2.4083
Ag_2Au_2	2.7754	4.5984	1.3877	0.3603	2.2992	0.0001
Ag_2Au_3	2.3672	4.0678	1.1836	0.4224	2.0339	2.4020
Ag_2Au_4	2.6937	4.6120	1.3468	0.3712	2.3060	1.9852
Ag_2Au_5	1.5509	4.1767	0.7754	0.6447	2.0883	0.0150
Ag_2Au_6	2.5305	4.9386	1.2652	0.3951	2.4693	2.6825
Ag_2Au_7	2.0135	4.3536	1.0067	0.4966	2.1768	2.2463
Ag_3Au	2.5577	3.9726	1.2788	0.3909	1.9863	2.0431
Ag_3Au_2	1.1972	5.1699	0.5986	0.8352	2.5849	2.0312
Ag_3Au_3	3.7005	4.8978	1.8502	0.2702	2.4489	0.0031
Ag_3Au_4	1.6598	4.2855	0.8299	0.6024	2.1427	0.0071
Ag_3Au_5	2.8842	5.1426	1.4421	0.3467	2.5713	0.0501
Ag_3Au_6	0.6258	4.5576	0.3129	1.5978	2.2788	2.2190
Ag_4Au	1.0067	4.4216	0.5033	0.9932	2.2108	2.3075
Ag_4Au_2	2.9114	4.8569	1.4557	0.3434	2.4284	0.0000
Ag_4Au_3	1.4693	4.0542	0.7346	0.6805	2.0271	2.1288

Ag_4Au_4	2.5849	4.9114	1.2924	0.3868	2.4557	0.0050
Ag_5Au	2.2856	3.8094	1.1428	0.4375	1.9047	0.6442
Ag_5Au_2	1.4693	3.8366	0.7346	0.6805	1.9183	0.0161
Ag_5Au_3	2.6937	4.7481	1.3468	0.3712	2.3740	2.6717
Ag_6Au	0.7074	3.3468	0.3537	1.4135	1.6734	0.0052
Ag_6Au_2	2.9658	4.9386	1.4829	0.3371	2.4693	2.9574
Ag_7Au	3.0203	5.0474	1.5101	0.3310	2.5237	0.7679

The linear regression analysis has been made between HOMO-LUMO energy gaps along with their computed softness in the Figure 1.

Figure 1: A linear correlation between Global Softness Vs HOMO-LUMO Gap

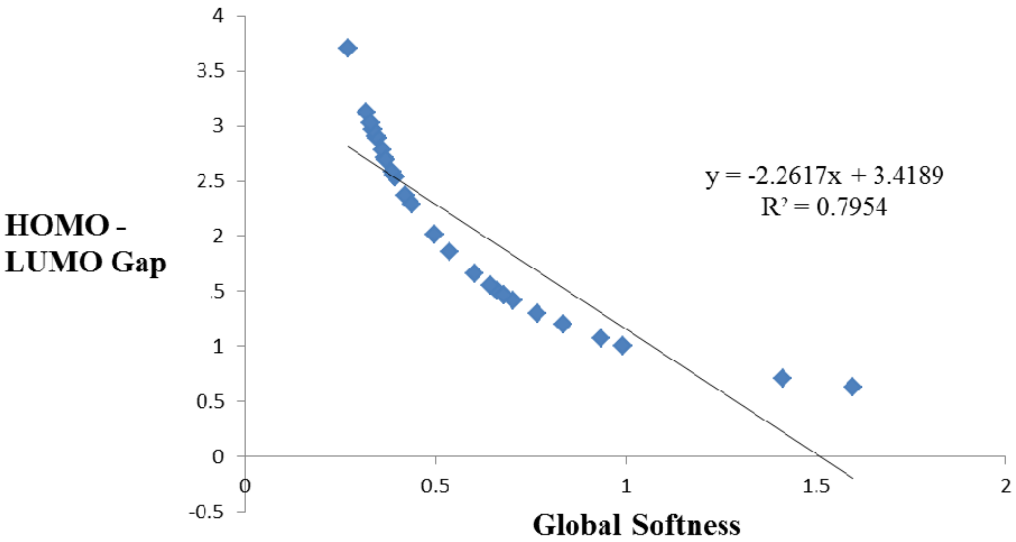

The nano alloy clusters of Ag_mAu_n; (m+n=2-8) have been parted in the form of $AgAu_n$ (n=1-7), Ag_nAu (n=1-7) and the remaining nano alloy clusters of Ag_mAu_n (m+n=2-8) like Ag_2Au_2, Ag_2Au_3, Ag_2Au_4 etc. to observe the behaviour of size dependence of the HOMO-LUMO energy gaps which are shown in the Figure -2, Figure-3 and Figure-4 respectively.

A comparative analysis of experimental and computed bond length is shown in Table 2.

Table 2: The calculated bond lengths (Å) for the Ag_2, Au_2, AgAu species

Species	Theoretical Bond Length	Experimental Bond Length^{REF}
Ag_2	2.50	2.53[61]
Au_2	2.48	2.47[62]
AgAu	2.50	2.50[36]

Figure 2: Size dependence of HOMO -LUMO Gap and $AgAu_n$; (n=1-7) nano alloy clusters

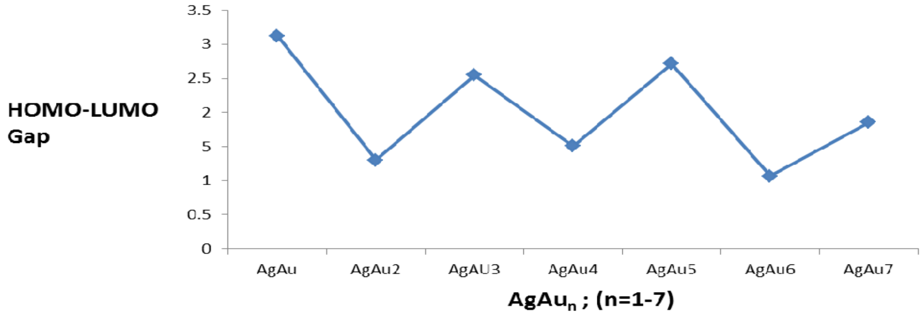

Figure 3: Size dependence of HOMO-LUMO Gap and Ag_nAu; (n=1-7) nano alloy clusters

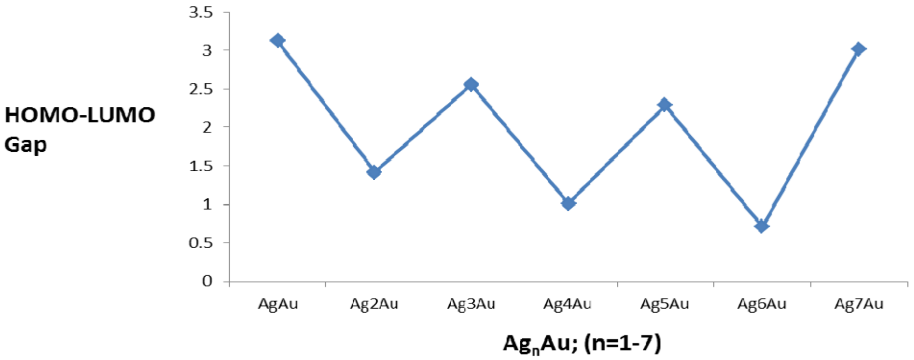

Figure 4: Size dependence of HOMO-LUMO Gap and Ag_mAu_n (Ag_2Au_2, Ag_2Au_3, Ag_2Au_4, Ag_2Au_5, Ag_2Au_6, Ag_2Au_7, Ag_3Au_2, Ag_3Au_3, Ag_3Au_4, Ag_3Au_5, Ag_3Au_6, Ag_4Au_2, Ag_4Au_3, Ag_4Au_4, Ag_5Au_2, Ag_5Au_3, Ag_6Au_3) nano alloy clusters

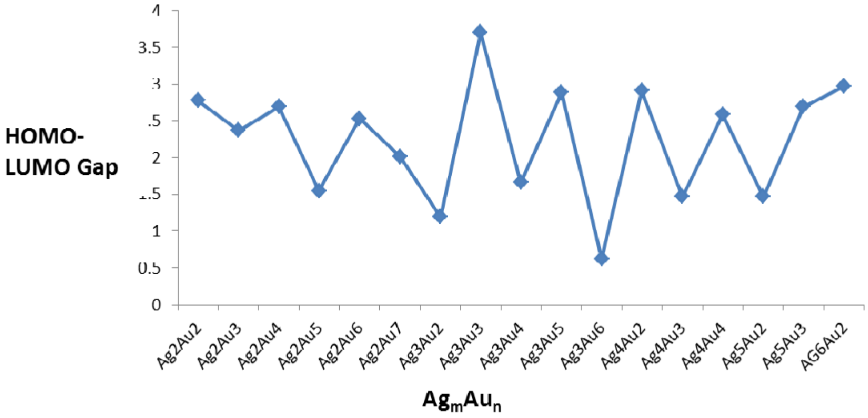

3.2. Discussion

From the Table 1, it is distinctly observed that HOMO-LUMO gaps of Ag-Au nano clusters maintain direct relationship with their computed global hardness values. As the frontier orbital energy gap increases, their hardness value increases. On experimental point of view this is expected. As the molecule possesses the highest HOMO-LUMO gap, it will be least prone to response against any external perturbation and that means it will be the least reactive. Table-1 reveals that Ag_3Au_3 is the least reactive species whereas Ag_3Au_6 will exhibit the maximum response. Though there is no such available quantitative data of optical properties of aforesaid clusters, we can assume that there must be a direct qualitative relationship between optical properties of Ag-Au nano clusters with their computed HOMO-LUMO gap. The assumption is based on the fact that optical properties of materials are interrelated with flow of electrons within the systems which in turn depend on the difference between the distance of valence and conduction band. A direct linear relationship between HOMO-LUMO gap with the difference in the energy of valence-conduction band has been already reported [60]. On the basis of above mentioned points, we may conclude that optical properties of instant bi-metallic Nano clusters increase with increase of their hardness values. Similarly softness data exhibits an inverse relationship towards the optical properties. The linear regression analysis has been made between HOMO-LUMO energy gaps along with their computed softness in the Figure – 1. The high value of regression coefficient observed in the Figure-1 (R^2=0.7954) validates our predicted model.

A comparative analysis has been made between experimental bond length [36, 61, 62] and our computed data of the species namely Ag_2, Au_2 and AgAu. The same is reported in Table-2. A close agreement between experimental report and our computed bond length is reflected form the Table -2. It supports and validates our computational analysis.

We have investigated the chemical stabilities of Ag_mAu_n; (m+n=2-8) in terms of energy gaps between HOMO-LUMO. It is observed that in a molecular system chemical stability is enhanced with large HOMO-LUMO energy gaps [63]. Figure-2, Figure-3 and Figure-4 reveals that the HOMO-LUMO energy gap for the nano alloy clusters exhibit remarkable odd-even oscillation behaviour, the even-number clusters show larger HOMO-LUMO energy gaps than the neighboring odd-number clusters, which is expected trend for closed/open systems [63, 64, 65, 66]. It has been already reported that the $Ag_{1,3,5,7}Au$ (even number) clusters keep higher chemical stability than their neighbor clusters (odd number). Same pattern is also visible in the Figure-2, Figure-3 and Figure-4 [63, 64, 65, 66]. The nano alloy clusters which show improved chemical stability can be used as building block of nanomaterials [63].

4. CONCLUSION

In recent day, bi-metallic nano alloy clusters have got immense importance due to its diverse nature of applications. A marked optical property is observed in case of nano cluster containing group 11 metals, namely Silver and Gold. In this paper, we have studied and analyzed for the first time about the molecular system of Ag_mAu_n; (m+n = 2-8) nano clusters interms of conceptual DFT based descriptors namely global hardness, electronegativity, softness, electrophilicity index and dipole moment. The result of this analysis reveals that the HOMO-LUMO gap of this alloy runs hand in hand along with it evaluated global hardness. As in absence of any quantitative benchmark, the optical property of Ag-Au nano cluster has been assumed to be exactly equivalence of it HOMO-LUMO gap. Here our evaluated data reveals that optical property of these compounds maintains a direct relationship with hardness and inverse relationship with softness. Considering other experimental facts, this trend is expected. The high numerical value of regression coefficients for different models, predicted between hardness, softness and HOMO-LUMO gap successfully supports our analysis. The nano alloy clusters also exhibit interesting odd-even oscillation behaviour, by showing that even numbers of clusters are more stable in comparison to their neighbor odd number clusters. From this study, we can say that Ag_3Au_3 is the most stable cluster among Ag_mAu_n (m+n=2-8) nano alloy clusters. Our computed bond lengths for the species like Ag_2, Au_2 and AgAu are numerically very close to the experimental values.

ACKNOWLEDGEMENT

S.V is very thankful to the management of Manipal University Jaipur, India for providing financial assistance. All the authors are thankful to the Manipal University Jaipur, India for providing research facilities.

REFERENCES

1. Khosousi, A. Z.; Dhirani, A. A. Charge transport in nanoparticle assemblies, *Chem. Rev.* **2008**,108, 4072-4124.
2. Daniel, M. C.; Astruc, D. Gold nanoparticles: assembly, supramolecular chemistry, quantum-size-related properties, and applications toward biology, catalysis, and nanotechnology, *Chem. Rev.* **2004**,104, 293-346.
3. Ghosh, S. K.; Pal, T. Interparticle coupling effect on the surface plasmon resonance of gold nanoparticles: from theory to applications, *Chem. Rev.* **2007**, 107, 4797-4862.
4. Chaudhuri, R. G.; Paria, S. Core/shell nanoparticles: Classes, properties, synthesis Mechanisms, characterization, and applications, *Chem. Rev.* **2012**, 112, 2373-2433.
5. Alivisatos, A. P. Semiconductor Clusters, Nanocrystals, and Quantum Dots, *Science* **1996,** 271, 933-937.
6. Kastner, M. A. Artificial Atoms, *Phys. Today* **1993,** 46, 24-31.
7. Haruta, M. Catalysis of Gold Nanoparticles Deposited on Metal Oxides**,** *Cattech* **2002**, 6, 102-115.
8. Ismail, R. Theoretical Studies of Free and Supported Nanoalloy Clusters. Ph.D Thesis, University of Birmingham, UK, 2012.
9. Roucoux, A.; Schulz, J.; Patin, H. Reduced transition metal colloids: A novel family of reusable catalysts?, *Chem. Rev.* **2002**, 102, 3757-3778.
10. Flores, B. M. M.; Kharisov, B. I.; Perez, V. M. J.; Martinez, P. E.; Lopez, S. T. Recent advances in the synthesis and main applications of metallic nano-alloys, *Ind. Eng. Chem. Res.* **2011**, 50, 7705-7721.

11. Murray, R. W. Nanoelectrochemistry: Metal Nanoparticles, Nanoelectrodes, and Nanopores, *Chem. Rev.* **2008**, 108, 2688-2720.
12. Teng, X.; Wang, Q.; Liu, P.; Han, W.; Frenkel, A. I.; Wen; Marinkovic, N.; Hanson, J. C.; Rodriguez, J. A. Formation of Pd/Au Nanostructures from Pd Nanowires via Galvanic Replacement reaction, *J. Am. Chem. Soc.* **2008**, 130, 1093-1101.
13. Ferrando, R.; Jellinek, J.; Johnston, R. L. Nanoalloys : from theory to applications of alloy clusters and nanoparticles, *Chem. Rev.* **2008**, 108, 845-910.
14. Henglein, A. Physicochemical properties of small metal particles in solution: "microelectrode" reactions, chemisorption, composite metal particles, and the atom-to-metal transition, *J. Phys. Chem.* **1993**, 97, 5457-5471.
15. Davis, S. C.; Klabunde, K. J. Unsupported Small Metal Particles: Preparation, Reactivity, and Characterization, *Chem. Rev.* **1982**, 82, 153-208.
16. Lewis, L. N. Chemical catalysis by colloids and clusters, *Chem. Rev.***1993**, 93, 2693-2730.
17. Schmid, G. Large clusters and colloids. Metals in the embryonic state, *Chem. Rev.* **1992**, 92, 1709-1727.
18. Schon, G.; Simon, U. A fascinating new field in colloid science: small ligand-stabilized metal clusters and possible application in microelectronics, *Colloid. Polym. Sci.* **1995**, 273, 101-117.
19. Oderji, H. Y.; Ding, H. Determination of melting mechanism of Pd< sub> 24</sub> Pt< sub> 14</sub> nanoalloy by multiple histogram method via molecular dynamics simulations, *Chem. Phys.* **2011**, 388, 23-30.
20. Liu, H. B.; Pal, U.; Medina, A.; Maldonado, C.; Ascencio, J. A. Structural incoherency and structure reversal in bimetallic Au-Pd nanoclusters, *Phys. Rev. B* **2005**, 71, 075403-075409.
21. Baletto, F.; Ferrando, R. Structural properties of nanoclusters: Energetic, thermodynamic, and kinetic effects, *Rev. Mod. Phys.* **2005**, 77, 371-423.
22. Alonso, J. A. Electronic and atomic structure, and magnetism of transition-metal clusters, *Chem. Rev.* **2000**, 100, 637-677.
23. Katakuse, I.; Ichihara, T.; Fujita, Y.; Matsuo, T.; Sakurai, T.; Matsuda, H. Mass Distributions of Copper,Silver and Gold Clusters and Electronic Shell Structure: I, *Int. J. Mass Spectrom. Ion Processes* **1985**, 67, 229-236.
24. Katakuse, I.; Ichihara, T.; Fujita, Y.; Matsuo, T.; Sakurai, T.; Matsuda, H. Mass Distributions of Negative Cluster Ions of Copper, Silver and Gold: I, *Int. J. Mass Spectrom. Ion Processes* **1986**, 74, 33-41.
25. Heer, W. A. D.; The physics of simple metal clusters: experimental aspects and simple models, *Rev. Mod. Phys.* **1993**, 65, 611-676.
26. Gantefor, G.; Gausa, M.; Broer, K. H. M.; Lutz, H. O. Photoelectron spectroscopy of silver and palladium cluster anions. Electron delocalization *versus*, localization, *J. Chem. Soc. Faraday Trans.***1990**, 86, 2483-2488.
27. Leopold, D. G.; Ho, J.; Lineberger, W. C. Photoelectron spectroscopy of mass-selected metal cluster anions. I. Cu_n^-, n=1-10, *J. Chem. Phys.***1987**, 86, 1715-1726.
28. Lattes, A.; Rico, I.; Savignac, A. D.; Samii, A. A. Z. Formamide, a water substitute in micelles and microemulsions xxx structural analysis using a diels-alder reaction as a chemical probe, *Tetrahedron* **1987**, 43, 1725-1735.

29. Chen, F.; Xu, G. Q.; Hor, T. S. A. Preparation and assembly of colloidal gold nanoparticles in CTAB-stabilized reverse microemulsion, *Mater. Lett.* **2003**, 57, 3282-3286.
30. Taleb, A.; Petit, C.; Pileni, M. P. Optical properties of self-assembled 2D and 3D superlattices of silver nanoparticles, *J. Phys. Chem. B* **1998**, 102, 2214-2220.
31. Deshpande, M. D.; Kanhere, D. G.; Vasiliev, I.; Martin, R. M. Density-functional study of structural and electronic properties of Na_nLi and Li_nNa (1<n<12) clusters, *Phys. Rev. A* **2002**, 65, 033202-1-6.
32. Dhavale, A.; Shah, V.; Kanhere, D. G. Structure and stability of Al-doped small Na clusters: Na_nAl (n=1,10), *Phys. Rev. A* 1998, 57, 4522-4527.
33. Zhao, G. F.; Sun, J. M.; Liu, X.; Guo, L. J.; Luo, Y. H. Geometries and electronic properties of Na_mSi_n(m+n>7) clusters, *J. Mol. Struct. Theochem* **2008**, 851, 348-352.
34. Zhang, X. R.; Gao, C. H.; Wu, L. Q.; Tang, H. S. The theory study of electronic structures and spectram properties of WnNim(n+m≤7; m=1, 2) clusters, *Acta Phys. Sin.* **2010**, 59, 5429-5442.
35. Wang, X. T.; Guan, Q. F.; Qiu, D. H.; Cheng, X. W.; Li, Y.; Peng, D. J.; Gu, Q. Q. Defect microstructures in polycrystalline pure copper induced by high-current pulsed electron beam--the vacancy defect clusters and surface micropores, *Acta Phys. Sin.* **2010**, 59, 7252-7257.
36. Fabbi, J. C.; Langenberg, J. D.; Costello, Q. D.; Morse, M. D.; Karlsson, L. Dispersed fluorescence spectroscopy of jet-cooled AgAu and Pt2, *J. Chem. Phys.* **2001**, 115, 7543-7549.
37. Weis, P.; Welz, O.; Vollmer, E.; Kappes, M. M. Structures of mixed gold-silver cluster cations (AgmAun+,m+n<6): Ion mobility measurements and density-functional calculations, *J. Chem. Phys.* **2004**, 120, 677-684.
38. Koutecký, V. B. Density functional study of structural and electronic properties of bimetallic silver-gold clusters: Comparison with pure gold and silver clusters, *J. Chem. Phys.* **2002**, 117, 3120-3131.
39. Langlois, C.; Wang, Z. W.; Pearmain, D.; Ricolleau, C.; Li, Z. Y. HAADF-STEM imaging of CuAg core-shell nanoparticles, *J. Phys.: Conference Series* **2010**, 241, 012043-012047.
40. Jankowaik, J. T. A.; Barteau, M. A. Ethylene epoxidation over silver and copper-silver bimetallic catalysts: I. kinetic and selectivity, *J. Catal.* **2005**, 236, 366-378.
41. Piccinin, S.; Zafeiratos, S.; Stampfl, C.; Hansen, T. W.; Hävecker, M.; Teschner D et al. Alloy catalyst in a reactive environment: The example of Ag-Cu particles for ethylene epoxidation, *Phys. Rev. Lett.* **2010**, 104, 035503-1-035503-4.
42. Wacker, O. J.; Kummel, R.; Gross, E. K. U. Time-dependent density- functional theory for superconductors, *Phys. Rev. Lett.* **1994**, 73, 2915-2918.
43. Illas, F.; Martin, R. L. Magnetic coupling in ionic solids studied by density functional theory *J. Chem. Phys.* **1998**, 108, 2519-2527.
44. Johnson, D.D.; Nicholson, D. M.; Pinski, F. J.; Gyorffy, B. L.; Stocks, G. M. Total-energy and pressure calculations for random substitutional alloys, *Phys. Rev. B* **1990**, 41, 9701-9716.
45. Kümmel, S.; Brack, M. Quantum fluid-dynamics from density functional theory, *Phys. Rev. A* **2001**, 64, 022506-022512.

46. Car, R.; Parrinello, M. Unified Approach for Molecular Dynamics and Density Functional Theory *Phys. Rev. Lett.* **1985**, 55, 2471-2474.
47. Koskinen, M.; Lipas, P.; Manninen, M. Shapes of light nuclei and metallic clusters, *Nucl. Phys. A* **1995**, 591, 421-434.
48. Schmid, R. N.; Engel, E.; Dreizler, R. M. Density functional approach to quantum hadrodynamics: Local exchange potential for nuclear structure calculations, *Phys. Rev. C* **1995**, 52, 164-169.
49. Chakraborty, T.; Ghosh, D. C. Correlation of the Drug Activities of Some Anti-Tubercular Chalcone derivatives in Terms of the Quantum Mechanical Reactivity Descriptors, *Int. J. Chemoinf Chem. Eng.* **2011,** 1, 53-65.
50. Chakraborty, T.; Ghosh, D. C. Correlation of the drug activities and identification of the reactive sites in the structure of some Anti-Tubuculour juglone derivatives in terms of molecular orbital and the density functional descriptors, *Int. J. Chem. Model.* **2012**, 4, 413-440.
51. Ranjan, P.; Kumar, A.; Chakraborty, T. Computational study of nanomaterials invoking DFT based descriptors, *Environmental Sustainability: Concepts, Principles, Evidenses and Innovations* , Mishra, G. M. Excelent Publishing House. New Delhi, India, 2014; Volume 1, pp. 239-242.
52. Ranjan, P.; Venigalla, S.; Kumar, A.; Chakraborty, T. A theoretical analysis of Bi-metallic Ag-Au_n , (n=1-7) nano alloy clusters invoking DFT based descriptors, *Research Methodology in Chemical Sciences: Experimental and Theoretical Approaches,* Chakraborty, T.; Ledwani, L., Apple Academic Press, USA, 2014 (in press).
53. Parr, R. G.; Yang, W. Density-Functional Theory of the Electronic Structure of Molecules, *Annu. Rev. Phy. Chem.* **1995**, 46, 701-728.
54. Kohn, W.; Becke, A. D.; Parr, R. G. Density Functional Theory of Electronic Structure, *J. Phys. Chem.* **1996**, 100, 12974-12980.
55. Liu, S.; Parr, R. G. Second-order density-functional description of molecules and chemical changes, *J. Chem. Phys.* **1997**, 106, 5578-5586.
56. Ziegler, T. Approximate density functional theory as a practical tool in molecular energetics and dynamics, *Chem.Rev.* **1991**, 91, 651-667.
57. Geerlings, P.; Proft, F. D. Chemical Reactivity as Described by Quantum Chemical Methods, *Int. J. Mol. Sci.* **2002**, 3, 276-309.
58. Gaussian 03, Revision C.02, Frisch M J, Trucks G W, Schlegel H B, Scuseria G E, Robb M A, Cheeseman J R, Montgomery J J A, Vreven T, Kudin K N, Burant J C, Millam J M, Iyengar S S, Tomasi J, Barone V, Mennucci B, Cossi M, Scalmani G, Rega, N, Petersson G A, Nakatsuji H, Hada M, Ehara M, Toyota K, Fukuda R, Hasegawa J, Ishida M, Nakajima T, Honda Y, Kitao O, Nakai H, Klene M, Li X, Knox J E, Hratchian H P, Cross J B, Bakken V, Adamo C, Jaramillo J, Gomperts R, Stratmann R E, Yazyev O, Austin A J, Cammi R, Pomelli C, Ochterski J W, Ayala P Y, Morokuma K, Voth G A, Salvador P, Dannenberg J J, Zakrzewski V G, Dapprich S, Daniels A D, Strain M C, Farkas O, Malick D K, Rabuck A D, Raghavachari K, Foresman J B, Ortiz J V, Cui Q, Baboul A G, Clifford S, Cioslowski J, Stefanov B B, Liu G, Liashenko A, Piskorz P, Komaromi I, Martin R L, Fox D J, Keith T, Al-Laham M A, Peng C Y, Nanayakkara A, Challacombe M, Gill P M W, Johnson B,

Chen W, Wong M W, Gonzalez C, and Pople J A, Gaussian, Inc., Wallingford CT, 2004.

59. Parr, R. G., Yang. W. *Density Functional Theory of Atoms and Molecules* Oxford University Press, Oxford 1989.
60. Xiao. H.; Kheli, J. T.; Goddard, W. A. III. Accurate Band Gaps for Semiconductors from Density Functional Theory, *J. Phys. Chem. Lett.* **2011**, 2, 212-217.
61. Beutel, V.; Kramer, H. G.; Bhale, G. L.; Kuhn, M.; Weyers, K.; Demtroder, W. High-resolution isotope selective laser spectroscopy of Ag_2 molecules, *J. Chem. Phys.* **1993**, 98, 2699-2708.
62. Huber, K. P.; Herzberg, G. *Constraints of Diatomic Molecules*, Van Nostrand Reinhold Company, New York 1979.
63. Li-Ping, D.; Xiao-Yu, K.; Peng, S; Ya-Ru, Z.; Yan-Fang, L. A comparative study of geometries, stabilities and electronic properties between bimetallic Ag_nX (X=Au, Cu; n=1-8) and pure silver clusters, *Chinese Phys B.* **2012**, 21, 043601-13.
64. Hakkinen, H.; Landman, U. Gold clusters (Au_N, $2 \leq N \leq 10$) and their anions, *Phys. Rev*. **2000**, 62, 2287-90.
65. Xi-Bo, Li.; Hong-Yan, Wang.; Xiang-Dong, Yang.; Zheng-He, Zhu.; Yong-Jian, Tang. Size dependence of the structures and energetic and electronic properties of gold clusters, *J. Chem. Phys*. **2007**, 126,084505.
66. Jain, P. K. A DFT- based study of the low-energy electronic structures and properties of small gold clusters, *Struct. Chem*., **2005**, 16, 421-426.

NEW FRONT. CHEM. (**2014**)
Volume 23, Number 2, pp. 123-130
ISSN 2393-2171; ISSN-L 2393-2171
© West University of Timișoara

Former: Ann. West Univ. Timisoara – Series Chem.
ISSN: 1224-9513

Article

COMPUTATIONAL STUDY ABOUT CYTOTOXICITY OF METAL OXIDE NANOPARTICLES INVOKING NANO-QSAR TECHNIQUE

***Srujana Venigalla*[1], *Seema Dhail* [2], *Prabhat Ranjan* [3], *Shalini Jain* [4], *Tanmoy Chakraborty* [5]♣**
[1,2,4,5] Department of Chemistry, Manipal University Jaipur; [3] Department of Mechatronics Engineering, Manipal University Jaipur-303007, India

ABSTRACT

Nano compounds are highly ranked in the research domain due to their remarkable structural aspects and other physical properties. Now a days, metallic oxides nanoparticles are being used in renewable energy, water treatment, food & agriculture, textiles, medical, electronics, photo-physical, cosmetics, pharmaceutical, automobiles and many other fields. Apart from their huge beneficial aspects, cytotoxic effects of these nano-sized compounds are widely reported. In the present analysis, a group of 17 metal oxides nanoparticles have been studied invoking conceptual Density Functional Theory (DFT) based descriptors. Experimental cytotoxicity is explained qualitatively in terms of our computed data. Nano- QSAR modelling has been performed using multi linear regression analysis between experimental toxicity and evaluated theoretical descriptors. A high value of regression coefficient explains efficacy of our predicted model.

Keywords: DFT, Cytotoxicity, multi linear regression, nano metal-oxide

1. INTRODUCTION

Nano compounds (of size 1-100nm) have captivated the researchers' attention due to their novel properties and advantages over macro and micro counterparts of a chemical compound. From the literature, it is known that the size of a chemical compound plays a major role in the bio-activity. Nanoparticles were reported with greater pharmacological activity even with reduced drug dose owing to their surface properties [1, 2]. Formulation

---

♣ Correspondent author: Dr. Tanmoy Chakraborty, Tel:0141-3999-100, Extn.:274, Fax:, E-mails:tanmoy.chakraborty@jaipur.manipal.edu; tanmoychem@gmail.com

of nano drugs or chemicals is a simple task when compared to assessing their biological activity. Determination of biological activity of a chemical compound is necessary when a new chemical is discovered from nature. Estimation of biological activity, determining effective dose range and safety consumes a lot of time involving animal models and human volunteers' clinical trials. Long-term toxic effects of a chemical are difficult to trace out even in the clinical trials as the probable reactions in the body may not be observed immediately after a compound enters the biological system. Significantly, quantitative structure activity relationship (QSAR) is helpful in reducing the time and cost spent for the studies. These nanoparticles are used in vast number of products now-a-days to improve the performance of manufactured goods. Unfortunately, these incorporated nanoparticles are causing toxic effects in a variety of biotic components either by dermal contact or inhalation or by ingestion [3-5]. Recently it was reported that silver nanoparticles used in various manufactured goods are the reason for toxic effects in some aquatic organisms [6] due to their gradual leaching from goods to the environment. Autopsy was reported in a person on heavy exposure to titanium dioxide nanoparticles for prolonged period of time. Similarly particles from various manufactured products have been causing toxic effects in biotic components of the environment. Experimental results from the previous researches are helpful in correlating the activity with the predicted values in in-silico drug design. In-silico drug design is a tool of bio-chemoinformatics where the physico-chemical properties of chemical compounds are determined computationally invoking descriptors. QSAR/QSPR approach plays important role in the determination of activity of a chemical compound. Owing to the size, nanoparticles are more potent and a maximum concentration of the dose is absorbed and distributed in the biological system. Biological systems exposed for prolonged period with nanoparticles are proved toxic. Metal oxide nanoparticles are used in various manufactured products intended for the biological use. Prolonged exposure of these particles causes various toxic effects including cancers [7, 8]. Determining toxic effects of the chemicals at a target site of biological system is not transparent and the effects may not be completely screened. Computational techniques are paramount in screening various effects of the chemical substance in the biological systems, which reduces the experimental costs and consumes time. QSAR/QSPR approach can be utilised to forecast the physicochemical behaviour of the nano compounds which are not yet synthesised. Descriptors play a major role in this approach; mathematically relates the structure and activity/property of a compound. Validation of QSAR/QSPR approach is important for the results to be acceptable. In the present study, metal oxides are optimised invoking Density functional theory (DFT) and Hartree-Fock (HF) method.

2. COMPUTATIONAL METHODOLOGY

17 metal oxide nanoparticles used in various marketed products were optimised in the present research work are listed in Table 1. Metal-oxide nanoparticles were optimised invoking DFT methodology using B3LYP functional, MPW1PW91 functional and LanL2MB basis set, 6-311G basis set. Descriptors were derived by ab-initio Hartree-fock method using LanL2DZ basis set and 6-311G basis set. The molecules are optimised to obtain the lowest energy state possible. The Eigen values obtained after optimisation were used to determine the Global properties i.e., Hardness (η), Softness (s), Electronegativity (χ), Electrophilicity index (ω) of the molecules. Derived global descriptors are correlated with the experimental activity to describe the level of correlation.

Despite the beneficial aspects of nanoparticles like improved bioavailability, increased surface area of particles is reported with cytotoxic effects [9] on prolonged exposure to the biological components. Cytotoxicity is an important property of the nano size metal-oxide rather than their macro and micro counterparts. Experimental in-vitro toxicity of nano sized metal oxides has been reported by Jerzy Leszczynski (Nature 2011). In-vitro studies of cytotoxicity were expressed in terms of logarithmic value of molar $1/EC_{50}$, given in Table 2 are expressed in mol l^{-1}.

Table 1: Computed DFT based Global Descriptors

No.	**Compound**	**Energy gap**	**Hardness (η)**	**Softness (S)**	**Electro-negativity (χ)**	**Electrophilicity index (ω)**
1	Al_2O_3	0.1288	0.0644	7.7627	0.1561	0.1892
2	Bi_2O_3	0.0869	0.0434	11.5114	0.1345	0.2084
3	CoO	0.0639	0.0319	15.6494	0.161	0.4056
4	Cr_2O_3	0.1239	0.062	8.0684	0.1541	0.1916
5	CuO	0.1454	0.0727	6.8766	0.1563	0.1681
6	Fe_2O_3	0.0464	0.0232	21.5424	0.1892	0.7711
7	In_2O_3	0.1372	0.0686	7.2896	0.1982	0.2865
8	La_2O_3	0.0666	0.0333	15.0060	0.1172	0.2063
9	NiO	0.0474	0.0237	21.0837	0.1777	0.6656
10	Sb_2O_3	0.1643	0.0822	6.0853	0.1216	0.0901
11	SiO_2	0.2182	0.1091	4.5837	0.2472	0.280
12	SnO_2	0.1552	0.0776	6.4432	0.1324	0.1129
13	TiO_2	0.0638	0.0319	15.6739	0.1683	0.4441
14	V_2O_3	0.0683	0.0341	14.650	0.1399	0.2864
15	Y_2O_3	0.0986	0.0493	10.140	0.1227	0.1526
16	ZnO	0.0865	0.0432	11.5674	0.1571	0.2855
17	ZrO	0.0496	0.0248	20.1653	0.1552	0.4856

All the molecules were optimised using Gaussian 03 package. Invoking Koopman's theorem, ionisation energy and electron affinity were calculated using the formulae,

$$I.E = -\varepsilon_{HOMO} \quad (1)$$

$$E.A = -\varepsilon_{LUMO} \quad (2)$$

Hence, ionisation energy and electron affinity are utilised to compute various global properties like hardness (η), softness (S), electronegativity (χ), electrophilicity index (ω) and chemical potential (μ):

$$\eta = (IE - EA)/2 \quad (3)$$

$$S = 1/2\eta \tag{4}$$

$$\chi = -\mu = (IE + EA)/2 \tag{5}$$

$$\omega = \chi^2/2\eta \tag{6}$$

The observed activity parameters; the global properties were given in Table 1 and Table 2. All the parameters are expressed in electron volts (eV).

Table 2: Computed descriptors invoking HF method

S. No	**Compound**	**Energy gap**	**Hardness (η)**	**Softness (S)**	**Electro-negativity (χ)**	**Electro-philicity index (ω)**	**Exper-imental activity (mol L^{-1})**
1	Al_2O_3	0.4066	0.2033	2.459	0.2212	0.1203	2.49
2	Bi_2O_3	0.2117	0.1058	4.7216	0.1025	0.0496	2.82
3	CoO	0.3227	0.1613	3.0990	0.1622	0.0815	3.51
4	Cr_2O_3	0.2731	0.1365	3.6613	0.1704	0.1063	2.51
5	CuO	0.3265	0.1632	3.0625	0.1259	0.0485	3.20
6	Fe_2O_3	0.0848	0.0424	11.7896	0.1743	0.3580	2.29
7	In_2O_3	0.4095	0.2047	2.4421	0.2029	0.1005	2.81
8	La_2O_3	0.2331	0.1165	4.2894	0.1102	0.0521	2.87
9	NiO	0.3054	0.1527	3.274	0.1704	0.0950	3.54
10	Sb_2O_3	0.4044	0.2022	2.4723	0.1179	0.0344	2.64
11	SiO_2	0.4998	0.2496	2.0025	0.2507	0.1259	2.20
12	SnO_2	0.4411	0.2205	2.2673	0.1815	0.0747	2.01
13	TiO_2	0.3639	0.1819	2.748	0.1933	0.1027	1.74
14	V_2O_3	0.3585	0.1792	2.790	0.1837	0.0942	3.14
15	Y_2O_3	0.3148	0.1574	3.1761	0.1803	0.1032	2.87
16	ZnO	0.3153	0.1576	3.1715	0.1752	0.0973	3.45
17	ZrO	0.3224	0.1611	3.1018	0.1811	0.1017	2.15

Multi linear regression analysis (MLR)

Global descriptors computed invoking DFT and HF-method were correlated with the experimental activity of the compounds (log $1/EC_{50}$) using minitab 16 statistical software. Testing of regression analysis revealed that the methods were approximate.

3. APPLICATION/RESULTS AND DISCUSSION

3.1. Results

17 metal-oxide compounds were optimised invoking Density functional theory and Hartree-Fock method. Optimisation of a chemical compound yields Eigen values which were used to compute energies of HOMO (highest occupied molecular orbital) and LUMO (lowest occupied molecular orbital) and inturn global properties like Hardness (η), Softness (s), Electronegativity (χ), Electrophilicity index (ω). Invoking Koopmans theorem, Eq. 1 and 2 are used to compute ionisation energy (I.E) and electron affinity (E.A) of the compounds. Further, the energies obtained from Eq. 1 and 2 are used to

derive various global properties. All the computed global properties invoking DFT and HF method are listed in Tables 1 and 2.

3.2. Discussion

From DFT approach, Fe_2O_3, NiO and ZrO are observed with high softness values 21.5424eV, 21.0837eV and 20.1654eV. From HF-method, Fe_2O_3 nano-particles were observed with greater softness, 11.7896eV. High value of softness indicates greater reactivity of the nano compounds. Greater is the reactivity, greater is the potency as well as the cytotoxic effects of the material. Experimental activity of nano metal-oxides is found to be greater in case of NiO, CoO and ZnO with 3.54mol l^{-1}, 3.51mol l^{-1} and 3.45mol l^{-1} respectively.

Table 3: Comparison of regression equation testing with the experimental activity

Compound	Experimental activity	DFT	HF
Al_2O_3	2.49	3.3698	2.573
Bi_2O_3	2.82	3.0152	2.5075
CoO	3.51	3.4504	3.3147
Cr_2O_3	2.51	3.3309	2.4932
CuO	3.20	3.377	4.0917
Fe_2O_3	2.29	3.5828	-11.764
In_2O_3	2.81	4.1653	2.9694
La_2O_3	2.87	2.8283	2.9574
NiO	3.54	3.5512	2.9568
Sb_2O_3	2.64	2.638	4.6510
SiO_2	2.20	5.3102	2.0592
SnO_2	2.01	2.8772	3.4711
TiO_2	1.74	3.5334	2.972
V_2O_3	3.14	3.1632	3.142
Y_2O_3	2.87	2.7635	2.8486
ZnO	3.45	3.3892	2.9639
ZrO	2.15	3.4116	2.9094

To determine the accuracy of the theoretical analysis, multi linear regression is used. In MLR studies, all the theoretical descriptors were correlated with the experimental activity of the metal oxide yielding a regression equation and regression coefficient (R^2). Regression analysis for DFT has exhibited regression coefficient (R^2) of 0.933 and by HF method the R^2 was 0.918. A high value of regression coefficient validates our effort in correlating the theoretical data with their experimental counterparts. Testing of the regression equation was done by substituting the descriptors values in the equation for every metal oxide compound. The results obtained were approximately similar to the experimental values with some exceptional compounds like Fe_2O_3 and TiO_2 with much variance from the experimental value. The data is presented in Table 3. From testing, it has been observed that the values obtained by both DFT and HF method are approximately similar except in case of Fe_2O_3 by HF method. Fig 1 represents the graph which compares theoretical activity against the experimental activity.

Figure 1: Comparison of Experimental activity with theoretical activity invoking DFT and HF method.

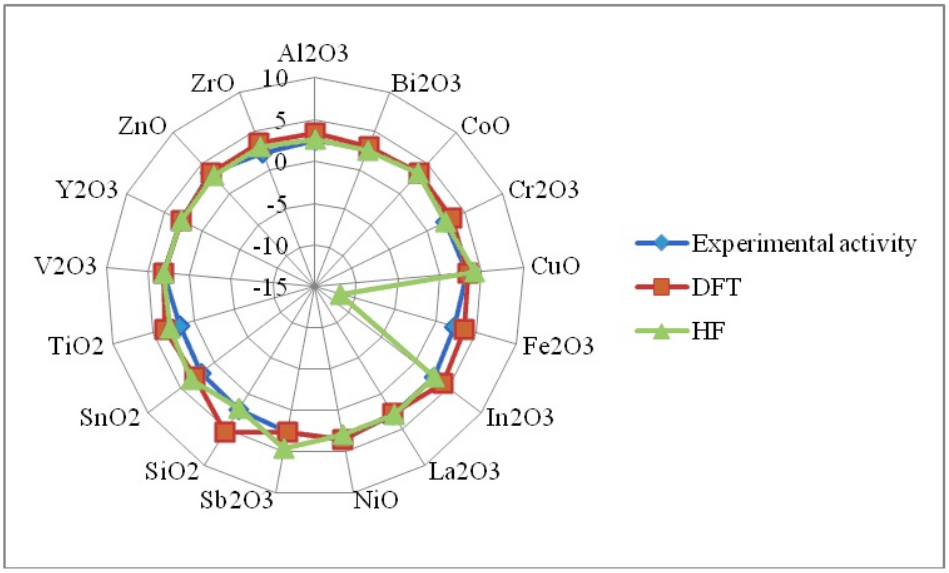

Here we have described as theoretical activity because, it is the activity obtained by substituting the descriptors in the regression equation. From the graph it is observed that the experimental activity of all the metal oxide compounds is merely correlating with the theoretical activity except in case of Fe_2O_3 Sb_2O_3 and SnO_2 using HF method.

4. CONCLUSION

In the present research, we have studied the toxicity of various nano metal oxide compounds used in various manufactured products. These manufactured products containing nano compounds may directly or indirectly come in contact with the biotic components and on prolonged exposure to these compounds yields toxic effects. So here, we have determined the activity in terms of the theoretical descriptors and correlated with the experimental activity and a nice correlation was observed. The values obtained invoking DFT and HF methods are almost similar and were approximately correlated with the experimental activity.

ACKNOWLEDGEMENT

One of the authors, S. Venigalla is very thankful to the management of Manipal University Jaipur for financial assistance with order no-MUJ/AS/00/20114-17. All the authors are very much thankful to Manipal University Jaipur for the research facilities.

REFERENCES

1. Marelli, B.; Ghezzi, C. E. Accelerated mineralization of dense collagen-nano bioactive glass hybrid gels increases scaffold stiffness and regulates osteoblastic function. Biomaterials 2011, 32, 8915–8926.
2. Singh, B.; Khurana, L. Development of optimized self-nano-emulsifying drug delivery systems (SNEDDS) of carvedilol with enhanced bioavailability. Drug Delivery 2011, 8, 599-612.
3. Leszczynski, J.; Rasulev, B. Using nano-QSAR to predict the cytotoxicity of metal oxides. NATURE NANOTECHNOLOGY 2011, 6, 175-178.
4. Yah, C. S.; Simate, G. S. Nanoparticles toxicity and their routes of exposures. Pak. J. Pharm. Sci 2012, 25, 477-499.
5. Huan, Y. W.; Aronstam, R.S. Toxicity of Transition Metal Oxide Nanoparticles: Recent Insights from in vitro Studies. Materials 2010, 3, 4842-4859.
6. Bianchini, A.; Wood, C.M. Mechanism of acute silver toxicity in Daphnia magna. Environmental Toxicology and Chemistry 2003, 22, 1361-1367.
7. Baun, A.; Hartmann, N. B. Ecotoxicity of engineered nanoparticles to aquatic invertebrates: a brief review and recommendations for future toxicity testing. Ecotoxicology 2008, 17, 387-395.
8. Xiong, D.; Fang, T. Effects of nano-scale TiO2, ZnO and their bulk counterparts on zebrafish: Acute toxicity, oxidative stress and oxidative damage. Science of The Total Environment 2011, 409, 1444–1452.
9. Maher, M.A; Naha, P.C. Numerical simulations of in vitro nanoparticle toxicity – The case of poly (amido amine) dendrimers. Toxicology in Vitro 2014, 28, 1449–1460.
10. Hadel, A; Enin, A. Nanotechnology - A Review article. Int. J. Pharm. Sci. Rev. Res. 2014, 29, 247-257.
11. Baun, A.; Hartmann, N.B. Toxicity and bioaccumulation of xenobiotic organic compounds in the presence of aqueous suspensions of aggregates of nano-C60. Aquatic Toxicology 2008, 86, 379–387.
12. Makarucha, A. J.; Todorova, N. Nanomaterials in biological environment: a review of computer modelling studies. Eur Biophys J. 2011, 40, 103-15.
13. Andrey, A; Toropov. QSAR model as a random event: A case of rat toxicity. Bioorganic & Medicinal Chemistry 2015, 23, 1223–1230.
14. Karelson, M.; Lobanov, V. S. Quantum-Chemical Descriptors in QSAR/QSPR Studies. ChemInform 2010, 27, 1027-1043.
15. Oberdörster, G.; Oberdörster, E. Nanotoxicology: An Emerging Discipline Evolving from Studies of Ultrafine Particles. Environ Health Perspect 2005, 113, 823–839.
16. Oberdörster, G. Safety assessment for nanotechnology and nanomedicine: concepts of nanotoxicology. J Intern Med. 2010, 267, 89-105.
17. Ghosh, D. C.; Chakraborty, T. Correlation of the Drug Activities of Some Anti-Tubercular Chalcone derivatives in Terms of the Quantum Mechanical Reactivity Descriptors. International Journal of Chemoinformatics & Chemical Engineering 2011, 1, 53-65.
18. Prabhat, R.; Chakraborty, T. Quantum mechanical study of some atomic properties. Journal of International Academy of Physical Sciences 2013, 17, 317-324.
19. Patel, T.; Telesca, D. Relating Nanoparticle Properties to Biological Outcomes in Exposure Escalation Experiments. Environmetrics 2014, 1, 57-68.

20. Sondra, S.; Teske. The Biomechanisms of Metal and Metal-Oxide Nanoparticles Interactions with Cells. Int. J. Environ. Res. Public Health 2015, 12, 1112-1134.
21. Guadagnini, R; Kenzaoui, B.H. Toxicity screenings of nanomaterials: challenges due to interference with assay processes and components of classic in vitro tests. Nanotoxicology 2013, doi:10.3109/17435390.2013.829590.
22. Ivask, A.; Kurvet, I. Size-Dependent Toxicity of Silver Nanoparticles to Bacteria, Yeast, Algae, Crustaceans and Mammalian Cells In Vitro. PLoS One 2014, 9, doi: 10.1371/journal.pone.0102108
23. Bondarenko, O.; Juganson, K. Toxicity of Ag, CuO and ZnO nanoparticles to selected environmentally relevant test organisms and mammalian cells in vitro: a critical review. Arch Toxicol 2013, 87, 1181-200.
24. Taylor, R. Interpretation of the Correlation Coefficient: A Basic Review. JDMS 1990, 1, 35-39.
25. Handy, R. D; Owen, R. The ecotoxicology of nanoparticles and nanomaterials: current status, knowledge gaps, challenges, and future needs. Ecotoxicology 2008, 17, 315-25.
26. Zhai, G.; Walters, K. S. Transport of gold nanoparticles through plasmodesmata and precipitation of gold ions in woody poplar. Environ Sci Technol Lett. 2014, 1, 146-151.
27. Glenn, J. B.; White, S. A. Interactions of gold nanoparticles with freshwater aquatic macrophytes are size and species dependent. Environ Toxicol Chem. 2012, 31, 194-201.
28. Attwood, S. T; Unrine, J. M. Uptake, distribution and toxicity of gold nanoparticles in tobacco (Nicotiana xanthi) seedlings. Nanotoxicology 2012, 6, 353-60.
29. Judy, J. D.; Unrine, J. M. Bioaccumulation of gold nanomaterials by Manduca sexta through dietary uptake of surface contaminated plant tissue. Environ Sci Technol. 2012, 46, 12672-8.
30. Ranjan, P.; Venigalla, S; Kumar, A.; Chakraborty, T. Research Methodology in Chemical Sciences: Experimental and Theoretical Approaches. CRC Press, Apple Academic Press (2014), (Book Chapter Accepted).
31. Kim, I. S.; Choi, S. J. Comparative Cytotoxicity of Al2O3, CeO2, TiO2 and ZnO Nanoparticles to Human Lung Cells. Journal of Nanoscience and Nanotechnology 2010, 10, 3453-3458.
32. Mukherjee, A.; Sabat, D. Cytotoxicity of Al2O3 Nanoparticles at Low Exposure Levels to a Freshwater Bacterial Isolate. Chem. Res. Toxicol. 2011, 24, 1899–1904.
33. Grimme, S.; Antony, J. A consistent and accurate ab initio parametrization of density functional dispersion correction (DFT-D) for the 94 elements H-Pu. J.Chem. Phys. 2010, 132, 154104.

NEW FRONT. CHEM. (**2014**)
Volume 23, Number 2, pp. 131-140
ISSN 2393-2171; ISSN-L 2393-2171

Former: Ann. West Univ. Timisoara – Series Chem.
ISSN: 1224-9513

Article

NON-ALCOHOLIC FATTY LIVER DISEASE: RELATION WITH THE CARDIOVASCULAR RISK

D.M. Duda-Seiman(1),(♣) ***, I. Mihai***(2,3)***, B. Bumbăcilă***(4)***, B. Petcov***(5)***,***
C. Duda-Seiman(6)***, A.G. Kolozsvari***(6)
[1] University of Medicine and Pharmacy "Victor Babeş" Timişoara, Dep. Of Cardiology, Discipl. of Ambulatory Internal Medicine, Prevention and Cardiovascular Rehabilitation
[2] County Hospital Timisoara
[3] Dr. Mihai Carmen Family Medicine Practice, Orţişoara, Timiş County
[4] DARIFARM Pharmacy, Sânandrei, Timiş County
[5] ASCAR Hospital Timişoara
[6] West University Timisoara, Laboratory of Structural and Computational Physical-Chemistry for Nanosciences and QSAR, Dep. of Biology-Chemistry

ABSTRACT

The purpose of this research study is to assess the presence of metabolic cardiovascular risk factors (lipid dismetabolismul, diabetes mellitus type 2), anthropometric (obesity) and smoking in subjects with and without steatosis (non-viral and non-alcoholic) and the influence of steatosis on cardiovascular risk. Subjects were examined by abdominal ultrasonography under á jeun conditions of at least 5 hours. Abdominal ultrasounding is the most commonly used method for detecting steatosis, is widespread and reproducible. Non-alcoholic fatty liver viewed on ultrasounds shows a bright echostructure (comparable to the kidneys) with a posterior attenuation of the signal and a blurred vascular hepatic drawing. In the light of these recommendations, assessment of non-HDL cholesterol levels contributes to a more accurate stratification of cardiovascular risk than the calculation of LDL cholesterol. The target level of non-HDL-cholesterol is with 30 mg/dL higherr than the corresponding target level of LDL - cholesterol.

Keywords: cardiovascula risk, liver dissease

♣ Corresponding author: University of Medicine and Pharmacy "Victor Babeş" Timişoara, Dep. Of Cardiology, Discipl. Of Ambulatory Internal Medicine, Prevention and Cardiovascular Rehabilitation, 49 C.D. Loga Av, Timişoara, Romania; email: dannymduda@yahoo.com

1. INTRODUCTION

Non-alcoholic hepatic steatosis (NASH) or non-alcoholic fatty liver (non alcoholic fatty liver disease - NAFLD) is an advanced stage of non-alcoholic fatty liver, more specifically, to extra fat is added an inflammatory component, which increases the risk of cardiovascular disease and of cardiovascular and overall mortality [1].

In the last years, the disease has reached epidemic proportions and it is considered the most common cause of chronic liver disease in Western countries. Approximately 20-30% of the adults in western countries suffer from non-alcoholic steato-hepatitis. The prevalence increases to 70-90% among people who are obese or have diabetes [2]. Recently, a growth of healthcare costs for patients with NAFLD by 26% was estimated and this does not exclude the possibility that it will become the leading cause of liver transplant in 2020, without considering the complications associated with NAFLD related to diabetes and the cardiovascular disease.

Close correlations between non-alcoholic fatty liver, abdominal obesity and insulin resistance are making difficult an indication of the exact cause of determinant factors of cardiovascular risk in patients with NAFLD. The liver is a target to system disorders as well as it is a source of pro-atherogenic molecules that enhance arterial damage [3].

NAFLD can be regarded as a hepatic manifestation of the metabolic syndrome defined by central obesity, hypertension, hypertriglyceridemia, low HDL cholesterol, and hyperglycemia [4].

The purpose of this research study is to assess the presence of metabolic cardiovascular risk factors (lipid dismetabolismul, diabetes mellitus type 2), anthropometric (obesity) and smoking in subjects with and without steatosis (non-viral and non-alcoholic) and the influence of steatosis on cardiovascular risk.

2. METHODS

The present study included 50 hypertensive consecutive patients (34 women, 16 men) with no documented atherothrombotic cardiovascular disease, who were asking for family doctor periodic control. Blood pressure was measured according to standard recommendations, and high pressure was defined as the registered values over 140/90 mmHg or pre-existing blood pressure - lowering medication [5]. Weight status was assessed by calculating body mass index (BMI) and waist circumference measurements. Overweight and obesity were defined by a BMI ≥ 25 kg/m^2 and ≥ 30 kg/m^2 [6]. Lipid metabolic parameters (total cholesterol - TC, triglycerides - TG, high density lipoprotein - HDL) and glucose were evaluated á jeun using a Reflotron device. The level of low-density lipoprotein - LDL was calculated using Friedewald's formula (the calculation cannot be carried out for triglyceride levels over 400 mg / dL) [7] :

$$\text{LDL [mg/dL]} = \text{CT [mg/dL]} - \text{HDL [mg/dL]} - \text{TG [mg/dL]}/5$$

Non-HDL cholesterol was estimated by the difference between total cholesterol level and serum HDL-cholesterol level [8]. Patients who were currently or have attended in the last year to normolipemiant treatments were excluded. The presence of type 2 diabetes was taken from patient records by medical letters previously issued by the diabetes doctors.

For each subject we estimated the risk of fatal cardiovascular event in the next 10 years using the SCORE system, the version online [9]. To achieve the purposed goal, we hypothesized that all subjects enrolled had a measured systolic blood pressure of 140 mmHg. Subjects with SCORE risk <1% had a low absolute cardiovascular risk, the risk score between 1 and 5% (inclusive) had moderate cardiovascular risk, subjects with SCORE risk between 5 and 10% (inclusive) recorded a high cardiovascular risk, and those with a SCORE risk over 10% had very high cardiovascular risk [6].

Subjects were examined by abdominal ultrasonography under á jeun conditions of at least 5 hours. Abdominal ultrasounding is the most commonly used method for detecting steatosis, is widespread and reproducible. Non-alcoholic fatty liver viewed on ultrasounds shows a bright echostructure (comparable to the kidneys) with a posterior attenuation of the signal and a blurred vascular hepatic drawing. These characteristics have a diagnostic sensitivity to non-alcoholic liver steatosis of 82 to 94% and a specificity of more than 82%. The discrimination power of the ultrasound method is much lower than senior imaging methods (computer tomography, magnetic resonance imaging) in focal lesions of hepatic steatosis [10]. The gold standard in hepatosteatosis diagnosis is liver biopsy, the absence of this being one of the limitations of the study. Enrolled patients completed a questionnaire on lifestyle: those who reported drinking were excluded. Smokers were considered those who said they smoked at least 10 cigarettes daily. Continuous variables were expressed as mean ± standard deviation. Comparisons were performed using unpaired Student's T test. To calculate the likelihood, logistic regression was used. P values < 0.05 were considered significant. Statistical analyzes were performed using Epi Info 6 software (version 6.04d, CDC - USA , WHO Geneva - Switzerland).

3. RESULTS AND DISCUSSIONS

3.1. Results

There were included 50 consecutive hypertensive patients (34 women, 16 men) with no documented atherothrombotic cardiovascular disease, who were asking for family doctor regularly control. Basic characteristics of the patient group are shown in Table 1.

Table 1: Basic characteristics in the study group BMI-body mass index, TC-total serum cholesterol levels; TG-the level of triglycerides, HDL-blood levels of high density lipoprotein; LDL - low density lipoprotein serum level

Parameter	Mean value ± standard deviation
Age, years	60,46 ± 11,79
BMI, kg/m^2	31,17 ± 6,81
TC, mg/Dl	202,54 ± 50,71
TG, mg/Dl	152,44 ± 69,48
HDL, mg/dL	47,34 ± 12,49
LDL, mg/dl	125,72 ± 47,54
Non-HDL, mg/Dl	154,85 ± 49,95
TG/HDL	3,62 ± 2,29
Blood glucose level, á jeun, mg/dL	105,28 ± 33,66

Within this group of hypertensive patients with documented atherothrombotic cardiovascular disease reported to the condition of hypertension, the presence of dislipidemic metabolism is observed with slightly ascended fractions of the non-protective lipoprotein (LDL) . Mild obesity (grade I), as defined by the body mass index, appears to be a characteristic to the sample of the patients enrolled in the study. Also carbohydrate perturbed metabolism is objectified by á jeun blood glucose levels (105.28 ± 33.66 mg/dL). Smoking is an unhealthy habit met in 42 % of the subjects.

The absolute SCORE cardiovascular risk was assessed, using the Heart Score online project [9]. To report the SCORE risk to the condition of non-alcoholic fatty liver without taking into account the variation of hemodynamic status, SCORE risk calculation was performed considering for calculation in the equation the value of 140 mmHg for systolic blood pressure. It can be noted that the sample of patients enrolled in the study are exposed to a moderate level of absolute cardiovascular risk (4.18 % ± 2.97 %).

Abdominal ultrasonography examination revealed the presence hepatosteatosis in half of the patients taken into the study (Figure 1).

Figure 1: Hepatic steatosis presence in non-alcoholic patients from the study group

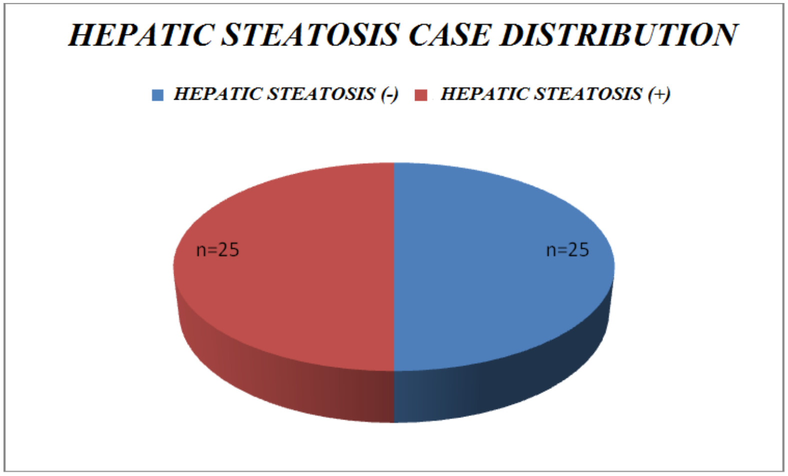

Elevated serum total cholesterol levels (≥ 190 mg/dL) are not predictive for the non-alcoholic steatosis condition: OR = 2.225 (95% CI, 0.7105 to 7.227, p = NS).

Correlation between total serum cholesterol level and the diagnosis of hepatic steatosis is shown in Table 2.

Table 2: Concordance between CT levels – hepatic steatosis in the study group

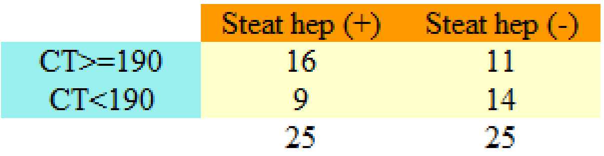

	Steat hep (+)	Steat hep (-)
CT>=190	16	11
CT<190	9	14
	25	25

Serum triglyceride levels above 150 mg/dL are an important and statistically significant relationship factor for the possibility of non-alcoholic fatty liver existence: OR =

15.41 (95% CI, 3.971 to 71.98, p = 0.000015). Correlation between serum triglyceride levels and diagnosis of hepatic steatosis is shown in Table 3.

Table 3: Concordance between TG levels and hepatic steatosis in the study group

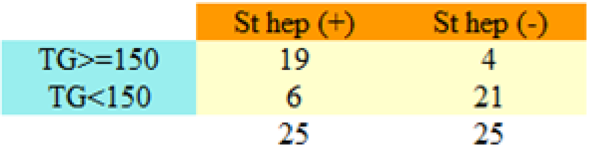

	St hep (+)	St hep (-)
TG>=150	19	4
TG<150	6	21
	25	25

Values above 100 mg/dL in serum LDL-cholesterol also cannot be placed in direct relation to the possibility of non-alcoholic hepatic steatosis: OR = 2.079 (95% CI, 0.6109 to 7.495, p = NS). Correlation between serum LDL cholesterol and hepatic steatosis diagnosis is shown in Table 4.

Table 4: Correlation between LDL levels and hepatic steatosis in the study group

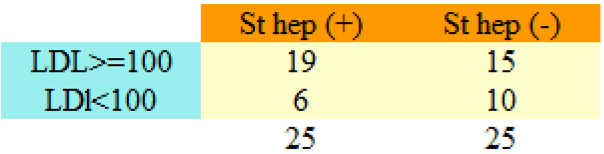

	St hep (+)	St hep (-)
LDL>=100	19	15
LDl<100	6	10
	25	25

Non-HDL cholesterol is significantly related to the possibility of non-alcoholic fatty liver: OR = 2.727 (95% CI, 0.8431 to 9.326, p = 0.0047). Correlation between non-HDL-cholesterol levels and the diagnosis of hepatic steatosis is shown in Table 5.

Table 5: Concordance between non-HDL and steatosis in the study group

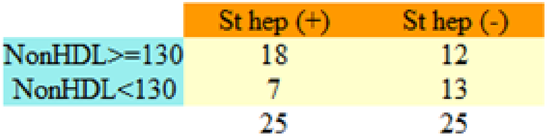

	St hep (+)	St hep (-)
NonHDL>=130	18	12
NonHDL<130	7	13
	25	25

A value of the ratio between serum triglyceride levels and low HDL-cholesterol value above 3 is a high and significantly predictive factor of fatty liver: OR = 4.422 (95% CI, 1.352 to 15.57, p = 0.0065). Concordance between the triglycerides / HDL-cholesterol ratio and hepatic steatosis diagnosis is shown in Table 6.

Contrary to expectations given by the results received from the relationship between lipid parameters and the chances of diagnosing non-alcoholic fatty liver, diabetes mellitus type 2 is not related to ultrasound diagnosis of fatty liver: OR = 2.213 (95% Cl, 0.6149 to 8.633, p = NS). Correlation between the presence of type 2 diabetes and hepatic steatosis diagnosis is shown in Table 7.

Table 6: Concordance between TG / HDL ratio and hepatic steatosis in the study group

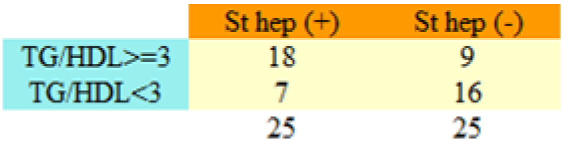

	St hep (+)	St hep (-)
TG/HDL>=3	18	9
TG/HDL<3	7	16
	25	25

Table 7: Concordance between type 2 diabetes and hepatic steatosis in the study group

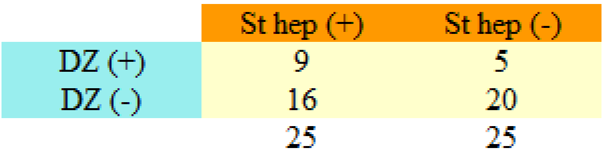

	St hep (+)	St hep (-)
DZ (+)	9	5
DZ (-)	16	20
	25	25

Smoking also cannot be related to ultrasound diagnosis of hepatic steatosis: OR = 2.263 (95% CI, 0.7132 to 7.482, p = NS). Concordance between the condition of smoking and diagnosis of hepatic steatosis is shown in Table 8.

Table 8: Concordance smoking - steatosis in the study group

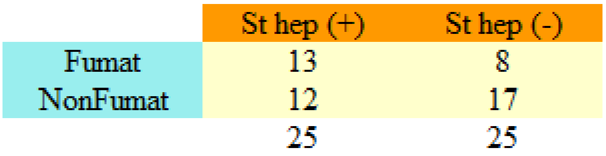

	St hep (+)	St hep (-)
Fumat	13	8
NonFumat	12	17
	25	25

A value of the SCORE absolute cardiovascular risk over 5% is not statistically significant with the possibility of correlation with ultrasound diagnosis of hepatic steatosis: OR = 0.4095 (95% CI, 0.1142 to 1.377, p = 0.07). Concordance between cardiovascular risk score and the diagnosis of hepatic steatosis is shown in Table 9.

Table 9: Concordance between the SCORE risk and hepatic steatosis in the study group

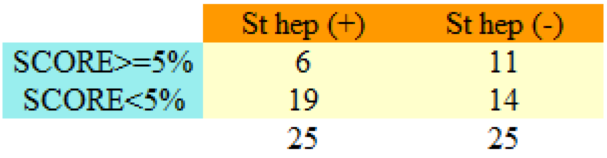

	St hep (+)	St hep (-)
SCORE>=5%	6	11
SCORE<5%	19	14
	25	25

3.2. Discussion

Non-alcoholic fatty liver is the most common cause of chronic liver disease in the general population living with "modern" habits, slowly progressing from simple fatty infiltration of liver (steatosis) with or without varying degrees of inflammation, to hepatocyte necrosis phenomena, fibrosis and ultimately cirrhosis [1]. Various studies have established that traditional cardiovascular risk factors are commonly encountered in subjects with various degrees of liver steatosis [11, 12]. However, there are parameters that are typically included in cardiovascular risk assessment scales, such as insulin resistance, obesity and elevated serum triglyceride levels, which are obviously changing the development of non-alcoholic fatty liver [13].

Intrahepatic triglyceride accumulation causes hepatic steatosis and this phenomena is favored by the presence of obesity. Obesity, defined by the body mass index is directly proportional to the prevalence of non-alcoholic fatty liver [14]. In our study, we found that obesity has a high prevalence in the group we had considered. Only two patients with non - alcoholic liver steatosis had a BMI in the normal range, 23 patients with liver steatosis entering in those overweighted or obese groups. It is important that structural and metabolic changes of liver to be captured from a young age so that targeted complex interventions can have the ability to correct the errors in the carbohydrate and lipid metabolisms. In a recent study, Deivanayagam et al. found significant association between weight status and altered fatty liver from adolescence with promoting insulin resistance and increased cardiovascular risk [15]. Weight reduction is beneficial for improving the liver histology (not for fibrosis).

Brutal reduction in body weight may be associated with a transient increase in fatty infiltration of the liver in parallel with transient increases in ALAT [16].

It has been shown that fatty liver is associated with changes in carbohydrate and lipid metabolisms. Furthermore, in vivo experiments have shown that hepatic steatosis causes insulin resistance [17]. In obese subjects, increased fat tissue determines the excretion of non - esterified fatty acids, glycerol, hormones, pro-inflammatory cytokines and other factors involved in the determinism of insulin resistance. Association with beta-pancreatic islets' dysfunction results the impossibility of glucose homeostasis, developing a type 2 diabetes [18]. Pro-inflammatory status conferred by the key link of non-alcoholic hepatic steatosis – the insulin resistance - underpins the development and evolution of the atherosclerotic process until the appearance of clinical events. In our study, type 2 diabetes was present almost exclusively in subjects with weight status modified: only one diabetic patient had normal weight. 9 of the 14 patients had been diagnosed with diabetic fatty liver by abdominal ultrasonography, results which overlap with data shown above in the current literature.

Recently it was pointed out that there is epidemiological evidence supporting that elevated levels of serum transaminases, elevations of gamma-glutamyl transpeptidase, documented morphological (by ultrasound assessment) of fatty liver and the presence of surrogate markers of liver fat infiltration may be associated with the development of type 2 diabetes [19].

Referring to the entire group of patients studied, mild hypertriglyceridemia was found to be a basic feature. The risk of developing non-alcoholic steatosis in hypertriglyceridemia basal conditions is over 4 times higher compared to the one in subjects without hypertriglyceridemia, with statistical significance. Recent studies have proven the validity of this relationship: hypertriglyceridemia is present in 64% of subjects with non-alcoholic liver steatosis and reduced HDL-cholesterol levels in 30-42% of subjects with non-alcoholic fatty liver [20, 21]. 90% of the subjects with non-alcoholic fatty liver have at least one risk factor for metabolic syndrome, and 33% are meeting all the criteria for the metabolic syndrome. [22]. As a result of these associations, it is reasonable to extrapolate the relationship between the non-alcoholic fatty liver and the cardiovascular risk. It was demonstrated an independent association between the presence of non-alcoholic fatty liver and the presence of carotid atherosclerotic plaques, endothelial dysfunction, relationship that retains statistical significance after adjusting for factors of metabolic syndrome components [23,24].

Ratios between serum levels of triglycerides and HDL and cholesterol with values of more than 3 are indicators of insulin resistance in subjects with weight status modified (in excess). In a recent study, in subjects of this type, the ratio TG / HDL ≥ 3 was associated with the risk of coronary events ($r^2 = 0.227$) in a much higher proportion than the components of metabolic syndrome taken separately or as a whole. The logarithm of the ratio TG / HDL (expression rate of the esterification of HDL - cholesterol) is in connection with the risk of coronary artery ($r^2 = 0.252$) [25]. Previously establishing the relationship between obesity and non-alcoholic hepatic steatosis, the ratio TG / HDL ≥ 3 can be used as a predictive factor for cardiovascular risk in such patients. The subjects in our study who had high ratio (over 3) have been also identified with fatty liver (OR = 4.422, 95 % CI, 1.352 to 15.57, p = 0.0065).

A recent study demonstrated that the increased ratio TG / HDL upraises the risk of first event coronary in each category of body mass index [26].

It is interesting to note that non-alcoholic fatty load of the liver in subjects taken in our study is related to the non-HDL-cholesterol: OR = 2.727 (95 % CI, 0.8431 to 9.326, p = 0.0047). Non - HDL cholesterol (calculated mathematically as the difference between total cholesterol and HDL-cholesterol) is a single measure of expression of the total atherogenic particles: lipoproteins containing apolipoprotein B (LDL, VLDL, IDL). It turned out that setting numerical value of non-HDL cholesterol is cost-effective compared to the direct determination of apolipoproteins B in determining the cardiovascular risk, especially in patients with levels of LDL cholesterol which are classifying the cardiovascular risk as "moderate" [27] impacting the practice of proper management of the cardiovascular risk factors and cardiovascular risk itself. According to recent recommendations [28], the non-HDL cholesterol is suitable to be calculated in the following situations:

- Patients with moderate hypertriglyceridemia (200-500 mg/dL);
- Patients with diabetes and/or coronary artery disease;
- Patients with insulin resistance syndrome.

4. CONCLUSIONS

In the light of these recommendations, assessment of non-HDL cholesterol levels contributes to a more accurate stratification of cardiovascular risk than the calculation of LDL cholesterol. The target level of non-HDL-cholesterol is with 30 mg/dL higherr than the corresponding target level of LDL - cholesterol.

In our study, no significant relationship was found between the absolute SCORE cardiovascular risk and the non-alcoholic liver steatosis. Identification of the non-alcoholic fatty liver (by abdominal ultrasonography) in hypertensive subjects with atherothrombotic cardiovascular disease should guide the practitioner to quantify potential secondary lipid targets that are directly related and independently with the absolute cardiovascular risk.

Further studies are needed to enroll a significant number of patients with non-alcoholic fatty liver disease, with a more diverse range of co-morbidities, to validate the hepatic morphological change as a cardiovascular risk marker.

REFERENCES

1. Bhatia, L.S.; Curzen, N.P.; Calder, P.C.; Byrne, C.D. Non-alcoholic fatty liver disease: a new and important cardiovascular risk factor? *Eur. Heart J.*, 2012, 33, (1190-1200).
2. Croke, B.; Sampson, D. Nonalcoholic fatty liver disease. Implications for clinical practice and health promotion. *Journal for Nurse Practitioners* **2012**, *8* (1), 45-50.
3. Targher, G.; Day, C.P.; Bonora, E. Risk of Cardiovascular Disease in Patients with Nonalcoholic Fatty Liver Disease. *N. Engl. J. Med.*, 2010, 363, (1341-1350).
4. Harmon, R.C.; Tiniakos, D.G.; Argo, C.K. Inflammation in Nonalcoholic Steatohepatitis. *Expert Rev. Gastroenterol. Hepatol.*, 2011, 2, (189-200).
5. The Task Force for the Management of Arterial Hypertension of Arterial Hypertension of the European Society of Hypertension (ESH) and of the European Society of Cardiology (ESC). 2007 Guidelines for the management of arterial hypertension. *Eur. Heart J.*, 2007, 28, (1462-1536).
6. The Fifth Joint Task Force of the European Society of Cardiology and Other Societies on Cardiovascular Disease Prevention in Clinical Practice (Constituted by representatives of nine societies and by invited experts). European guidelines on cardiovascular diseases prevention in clinical practice (version 2012). *Eur. Heart J.,* 2012, 33, (1635-1701).
7. Friedewald, W.T.; Levy, R.I.; Fredrickson, D.S. Estimation of the concentration of low-density lipoprotein cholesterol in plasma, without use of the preparative ultracentrifuge. *Clin. Chem.*, 1972, 18, (499-502).
8. The Emerging Risk Factors Collaboration. Major lipids, apolipoproteins, and risk of vascular disease. *JAMA*, 2009, 302 (18), (1993-2000).
9. Heart Score. The country-specific interactive tool for predicting and managing the risk of heart attack and stroke in Europe. URL www.escardio.org/HeartScore (accessed on 28 March 2015).
10. Choudhury, J.; Sanyal, A.J. Clinical aspects of fatty liver disease. *Semin. Liver Dis.*, 2004, 24 (4).
11. Gastaldelli, A.; Kozakova, M.; Hojlund, K.; Flyvbjerg, A.; Favuzzi, A.; Mitrakou, A.; Balkau, B. Fatty liver is associated with insulin resistance, risk of coronary heart disease, and early atherosclerosis in a large European population. *Hepatology* **2009**, *49*, 1537–1544.
12. Villanova, N.; Moscatiello, S.; Ramilli, S.; Bugianesi, E.; Magalotti, D.; Vanni, E.; Zoli, M.; Marchesini, G. Endothelial dysfunction and cardiovascular risk profile in nonalcoholic fatty liver disease. *Hepatology* **2005**, *42*, 473–480.
13. Khot, U.N.; Khot, M.B.; Bajzer, C.T.; Sapp, S.K.; Ohman, E.M.; Brener, S.J.; Ellis, S.G.; Lincoff, A.M.; Topol, E.J. Prevalence of conventional risk factors in patients with coronary heart disease. *JAMA*, 2003, 290, (898–904).
14. Ruhl, C.E.; Everhart, J.E. Determinants of the association of overweight with elevated serum alanine aminotransferase activity in the United States. *Gastroenterology* **2003**, 124, (71–79).
15. Deivanayagam, S.; Mohammed, B.S.; Vitola, B.E.; Naguib, G.H.; Keshen, T.H.; Kirk, E.P.; Klein, S. Nonalcoholic fatty liver disease is associated with hepatic and

skeletal muscle insulin resistance in overwight adolescents. *Am. J. Clin. Nutr.*, 2008, 88 (2), (257-262).

16. Andersson Friis-Liby, I.; Brandberg, J.; Gummasson, A.; et al. Weight reduction induces rapid changes in liver fat in obese patients with NAFLD and metabolic syndrome: a study by computerized tomography with short intervals. *Gastroenterology* **2005**, *128* (Suppl. 2), A-767.
17. Ibdah, J.A.; Perlages, P.; Zhao, Y.; Angdisen, J.; Borgerink, H.; Shadoan, M.K.; et al. Mice heterozygous for a defect in mitochondrial trifunctional protein develop hepatic steatosis and insulin resistance. *Gastroenterology* **2005**, *128*, 1381–1390.
18. Kahn, S.E.; Hull, R.L.; Utzschneider, K.M. Mechanisms linking obesity to insulin resistance and type 2 diabetes. *Nature* **2006**, *444*, 840-846.
19. Lattuada, G.; Ragogna, F.; Perseghin, G. Why does NAFLD predict type 2 diabetes? *Curr. Diab. Rep.*, 2011, 11, (167-172).
20. Marchesini, G.; Bugianesi, E.; Forlani, G.; et al. Nonalcoholic fatty liver, steatohepatitis, and the metabolic syndrome. *Hepatology* **2003**, *37*, 917–923.
21. Marchesini, G.; Marzocchi, R. Metabolic syndrome and NASH. *Clin. Liver Dis.*, 2007, 11, (105–117).
22. Kotronen, A.; Westerbacka, J.; Bergholm, R.; Pietilainen, K.H.; Yki-Jarvinen, H. Liver fat in the metabolic syndrome. *J. Clin. Endocrinol. Metab.*, 2007, 92, (3490–3497).
23. Paschos, P.;Paletas, K. Non alcoholic fatty liver disease and metabolic syndrome. *Hippokratia* **2009**, *13* (1), 9-19.
24. Volzke, H.; Robinson, D.M.; Kleine, V.; et al. Hepatic steatosis is associated with an increased risk of carotid atherosclerosis. *World J. Gastroenterol.*, 2005, 11, (1848–1853).
25. Marotta, T.; Russo, B.F.; Ferrara, A. Triglyceride-to-HDL-cholesterol ratio and metabolic syndrome as contributors to cardiovascular risk in overweight patients. *Obesity* **2010**, *18* (8), 1608-1613.
26. Cordero, A.; Andrés, E.; Ordóñez, B.; León, M.; Laclaustra, M.; Grima, A.; Luengo, E.; Moreno, J.; Bes, M.; Pascual, I.; Civeira, F.; Pocovi, M.; Alegría, E.; Casasnovas, J.A. Usefulness of triglycerides-to-high-density lipoprotein cholesterol ratio for predicting the first coronary event in men. *Am. J. Cardiol.*, 2009, 104 (10), (1393-1397).
27. Peters, A.L. Clinical relevance of non-HDL cholesterol in patients with diabetes. *Clinical Diabetes* **2008**, *26* (1), 3-7.
28. AACE Lipid and Atherosclerosis Guidelines. *Endocr. Pract.*, 2012, 18 (Suppl. 1), 1-78.

NEW FRONT. CHEM. (**2014**)
Volume 23, Number 2, pp. 141-147
ISSN 2393-2171; ISSN-L 2393-2171
© West University of Timișoara

Former: Ann. West Univ. Timisoara – Series Chem.
ISSN: 1224-9513

Article

A NEW VERSION OF ZAGREB INDEX OF CIRCUMCORONENE SERIES OF BENZENOID

Mohammad Reza Farahani **(♣)**
Department of Applied Mathematics, Iran University of Science and Technology (IUST), Narmak, 16844, Tehran, Iran

ABSTRACT

Let $G=(V,E)$ be a graph, where $V(G)$ is a non-empty set of vertices and $E(G)$ is a set of edges. One of the best known and widely used is Zagreb topological index M_1 introduced in 1972 by *Gutman* and *Trinajstić*. Recently (in 2012), we know two new version of First Zagreb index as $M^*_1(G)=\sum_{uv\in E(G)} (ecc(v)+ecc(u))$, that introduced by *Ghorbani* and *Hosseinzadeh* and $ecc(u)$ is the largest distance between u and any other vertex v of G. In this paper we compute this new topological index of Circumcoronene series of benzenoid H_k.

Keywords: Cut Method, Orthogonal Cut, Zagreb Topological index, Eccentricity Connectivity index, Molecular Graph, Circumcoronene series of benzenoid.

1. INTRODUCTION

All of the graphs in this paper are simple. A molecular graph is a simple graph such that its vertices correspond to the atoms and the edges to the bonds.

Mathematical chemistry is a branch of theoretical chemistry for discussion and prediction of the molecular structure using mathematical methods without necessarily referring to quantum mechanics. Chemical graph theory is a branch of mathematical chemistry which applies graph theory to mathematical modeling of chemical phenomena [1-3]. This theory had an important effect on the development of the chemical sciences.

A topological index of a graph is a number related to a graph which is invariant under graph automorphisms and is a numeric quantity from the structural graph of a molecule.

[♣] Correspondence: Tel: +98-919-247-8265,
E-mails: Mr_Farahani@Mathdep.iust.ac.ir & MrFarahani88@gmail.com

One of the best known and widely used is the Zagreb topological index M_1 introduced in 1972 by *I. Gutman* and *N. Trinajstić* and is defined as the sum of the squares of the degrees of all vertices of *G* [1,2].

$$M_1(G)=\sum_{v\in V(G)} (d_v)^2 \ or \ \sum_{e=uv\in E(G)} (d_u+d_v)$$

where d_u denotes the degree (number of first neighbors) of vertex u in *G*. Mathematical properties of the first Zagreb index for general graphs can be found in [4-8].

Recently, *M. Ghorbani* and *M.A. Hosseinzadeh* introduced a new version of first Zagreb index in 2012 [9] as follows:

$$M^*_1(G)=\sum_{e=uv\in E(G)} (\,ecc(v)_+ecc(u))$$

where *ecc(v)* is eccentricity of vertex *v*. Let $x,y\in V(G)$ then the distance *d(x,y)* between *x* and *y* is defined as the length of any shortest path in *G* connecting x and y [10-12].

In other words,

$$ecc(v)=Max\{d(u,v)|\,\forall u\in V(G)\}$$

In this paper, we call this index by *Third Zagreb index* as $M^*_1(G)=M_3(G)$ and compute this new topological index for Circumcoronene series of benzenoid H_k $(k\geq1)$. The Circumcoronene series of benzenoid is family of molecular graph, which consist several copy of benzene C_6 on circumference. Reader can see some first members of this family in Figure 1 and its structure in general case is shown in Figure 2 (see [13-24]).

Figure 1: Some first members of Circumcoronene series of benzenoid H_k $(k\geq1)$ [18-24].

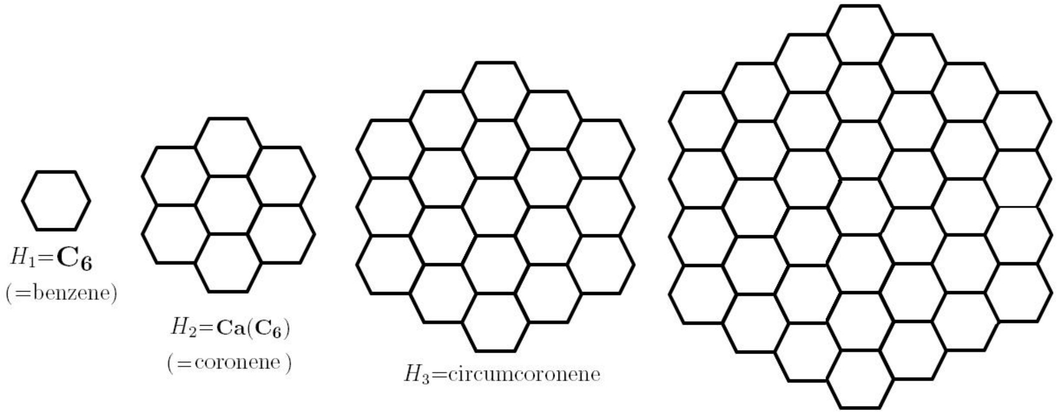

2. RESULTS AND DISCUSSION

In this sections, we compute the third Zagreb index $M_3(G)$ for Circumcoronene series of benzenoid H_k $\forall k\geq1$. For achieve to our aims, we use of Ring-cut Method. Definition of the Cut Method and some its properties are presented in [17].

We encourage readers that lock at to Figure 3 and see ring-cuts of Circumcoronene series of benzenoid, for example.

Figure 2: The Circumcoronene Series of benzenoid H_k $(k\geq 1)$ [18-24].

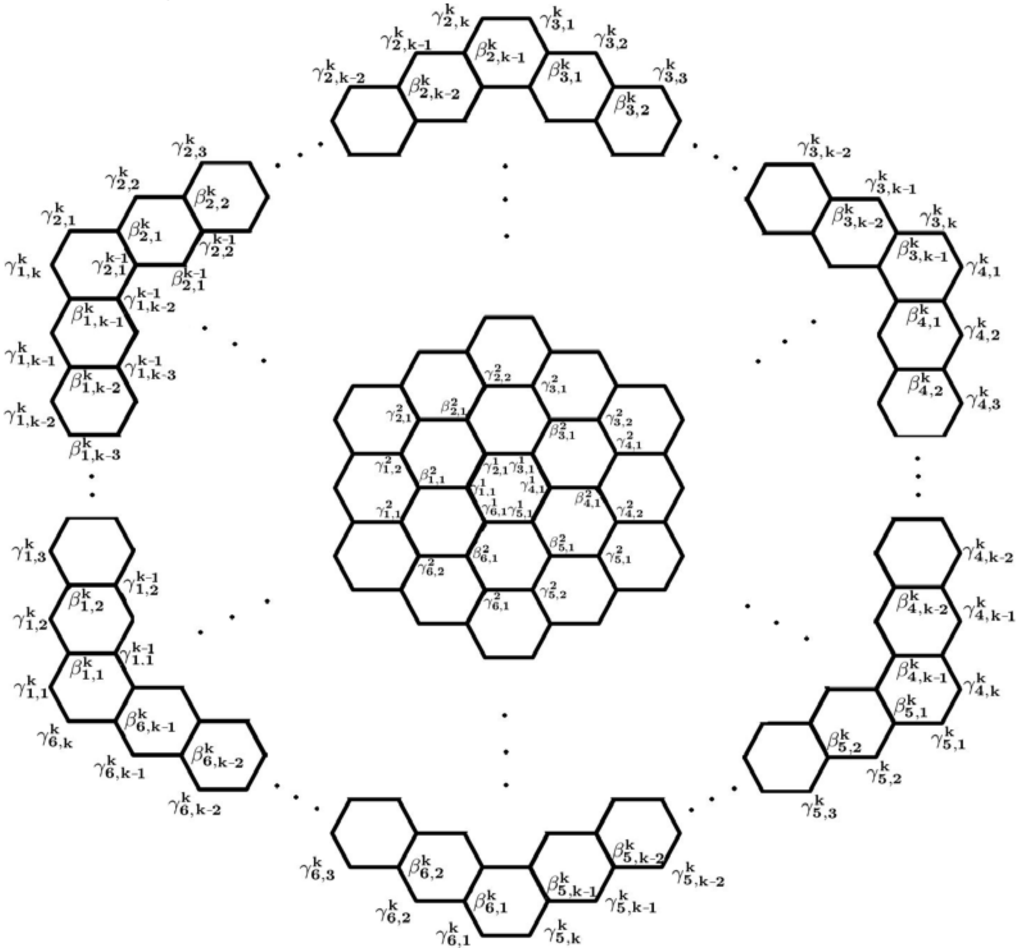

Now, we can exhibit the closed formula of third Zagreb index $M_3(H_k)$ in following theorem.

Theorem 1. The First Zagreb index of Circumcoronene series of benzenoid H_k $(k\geq 1)$ is equal to [24]

$$M_1(H_k)=54k^2-30k$$

Theorem 2. Let G be the Circumcoronene series of benzenoid H_k $(k\geq 1)$. Then the third Zagreb index of H_k is equal to

$$M_3(H_k)=60k^3-33k^2+9k$$

Proof of Theorem 2. Consider circumcoronene series of benzenoid G=Hk (k≥1), as shown in Figure 2. Here, we denote its vertices by following notations (At first, suppose $\mathbb{Z}6$ is the cycle finite group of order 6 and I coming from $\mathbb{Z}_k$):

1) Consider Benzene C6 (or sub-graph H_1 of H_k) and call vertices by $\gamma^1_{z,1}$ for every all z∈ $\mathbb{Z}_6$, respectively.

2) Name all $\gamma^1_{z,j}$'s adjacent vertices (without name) by $\beta^2_{z,j}$, such that j is constant (=1) and z∈$\mathbb{Z}_6$.

3) Name two remaining $\beta^2_{z,j}$'s adjacent vertices by $\gamma^2_{z,j}, \gamma^2_{z,j+1}$ (j=1, z∈ $\mathbb{Z}$6) such that edges $\beta^2_{z,j}\gamma^2_{z,j}, \beta^2_{z,j}\gamma^2_{z,j+1}$ be the in E(Hk); see Figure 3.

4) Name all $\gamma^i_{z,j}$'s adjacent vertices (without name) by $\beta^i_{z,j}$, such that j=1,…,I and j∈$\mathbb{Z}$i & z∈$\mathbb{Z}$6.

5) Name two remaining $\beta^i_{z,j}$'s adjacent vertices by $\gamma^i_{z,j}, \gamma^i_{z,j+1}$ such that j∈$\mathbb{Z}$i-1 & z∈$\mathbb{Z}$6 and insert two edges $\beta^i_{z,j}\gamma^i_{z,j}$, $\beta^i_{z,j}\gamma^i_{z,j+1}$ into E(Hk); see Figure 3.

Figure 3. The Ring-cuts of Circumcoronene series of benzenoid. [18-24].

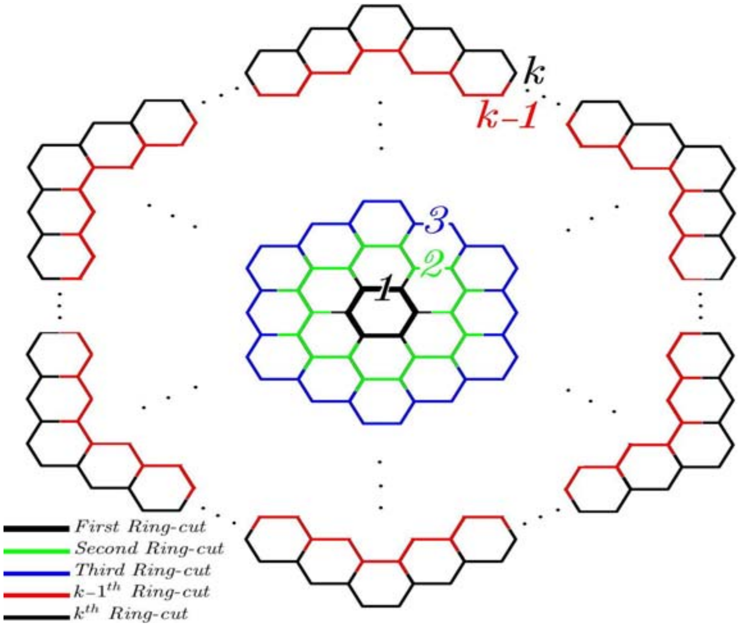

Thus, by above notations, the sets of vertices and edges of Circumcoronene series of benzenoid *G=H$_k$ (k≥1)* are equal to:

$$V(H_k)=\{V(H_k)=\{\gamma^i_{z,j},\beta^i_{z,l}\ |i\in\mathbb{Z}_k\ \&\ j\in\mathbb{Z}_i\ \&\ z\in\mathbb{Z}_6\},$$

$$E(H_k)=\{\beta^i_{z,j}\gamma^i_{z,j},\beta^i_{z,j}\gamma^i_{z,j+1},\beta^i_{z,j}\gamma^{i-1}_{z,j}\ and\ \gamma^i_{z,i}\gamma^i_{z+1,1}\,|i\in\mathbb{Z}_k\ \&\ j\in\mathbb{Z}_i\ \&\ z\in\mathbb{Z}_6\}.$$

Also, by attention to ring cuts of H_k in Figure 3 and using above notations, it had understood that all vertices where named in step I^{th} , conditions 4) and 5) above, are in I^{th} ring cut R_i of H_k. Thus, we using of results from [17] and conclude some properties as follow:

(I) $\forall i=1,\dots,k;\ j\in\mathbb{Z}_{i-1}\ \&\ z\in\mathbb{Z}_6$: $ecc(\beta^i_{z,j})=\underbrace{\mathbf{d}(\beta^{\mathbf{i}}_{\mathbf{z,j}},\beta^{\mathbf{i}}_{\mathbf{z+3,j}})}_{4i-3}+\underbrace{\mathbf{d}(\beta^{\mathbf{i}}_{\mathbf{z+3,j}},\gamma^{\mathbf{k}}_{\mathbf{z+3,j}})}_{2(k-i)+1}=2(k+i+1)$

(II) $\forall i=1,\dots,k;\ j\in\mathbb{Z}_i\ \&\ z\in\mathbb{Z}_6$: $ecc(\gamma^i_{z,j})=\underbrace{\mathbf{d}(\gamma^{\mathbf{i}}_{\mathbf{z,j}},\gamma^{\mathbf{i}}_{\mathbf{z+3,j}})}_{4i-1}+\underbrace{\mathbf{d}(\gamma^{\mathbf{i}}_{\mathbf{z+3,j}},\gamma^{\mathbf{k}}_{\mathbf{z+3,j}})}_{2(k-i)}=2(k+i)-1$

Therefore, we have following computations for third Zagreb index $M_3(H_k)$ as:

$$M^*_1(H_k)=\sum_{e=uv\in E(H_k)}(ecc(v)+ecc(u))\Rightarrow$$

$$\begin{aligned}M_3(H_k)=&\sum_{\beta^i_{z,j}\gamma^i_{z,j}\in \mathrm{E}(H_k)}[\mathrm{ecc}(\beta^i_{z,j})+\mathrm{ecc}(\gamma^i_{z,j})]+\sum_{\beta^i_{z,j}\gamma^i_{z,j+1}\in \mathrm{E}(H_k)}[\mathrm{ecc}(\beta^i_{z,j})+\mathrm{ecc}(\gamma^i_{z,j+1})]\\&+\sum_{\beta^i_{z,j}\gamma^{i-1}_{z,j}\in \mathrm{E}(H_k)}[\mathrm{ecc}(\beta^i_{z,j})+\mathrm{ecc}(\gamma^{i-1}_{z,j})]+\sum_{\gamma^i_{z,i}\gamma^i_{z+1,1}\in \mathrm{E}(H_k)}[\mathrm{ecc}(\gamma^i_{z,i})+\mathrm{ecc}(\gamma^i_{z+1,1})]\\&=\sum_{i=2}^{k}\sum_{j=1}^{i}\sum_{z=1}^{6}[\mathrm{ecc}(\beta^i_{z,j})+\mathrm{ecc}(\gamma^i_{z,j})]+\sum_{i=2}^{k}\sum_{j=1}^{i}\sum_{z=1}^{6}[\mathrm{ecc}(\beta^i_{z,j})+\mathrm{ecc}(\gamma^i_{z,j+1})]\\&+\sum_{i=1}^{k-1}\sum_{j=1}^{i}\sum_{z=1}^{6}[\mathrm{ecc}(\beta^{i+1}_{z,j})+\mathrm{ecc}(\gamma^i_{z,j})]+\sum_{i=1}^{k}\sum_{z=1}^{6}[\mathrm{ecc}(\gamma^i_{z,i})+\mathrm{ecc}(\gamma^i_{z+1,1})]\end{aligned}$$

Now, using properties (I) and (II) above, where $ecc(\beta^i_{z,j})=2k+2i-2$ and $ecc(\gamma^i_{z,j})=2k+2i-2$, respectively. Obviously $\sum_{z=1}^{6}1=6$.

$$
\begin{aligned}
M_3(H_k) &= 2\left(\sum_{i=2}^{k} 6(i-1)\left[2k+2i-1+2k+2i-2\right]\right)+\sum_{i=1}^{k-1} 6i\left[2k+2i-1+2k+2(i+1)-2\right]+\sum_{i=1}^{k} 6\left(4k+4i-2\right)\\
&= 2\left(\sum_{i=1}^{k-1} 6i\left(4k+4i+1\right)\right)+\sum_{i=1}^{k-1} 6i\left(4k+4i-1\right)+\sum_{i=1}^{k}\left(24k+24i-12\right)\\
&= \ldots\\
&= \sum_{i=1}^{k-1} 72i^2+\sum_{i=1}^{k-1}\left(72k+30\right)i+\sum_{i=1}^{k-1} (24k-12)+48k-12\\
&= 72\left(\frac{k(k-1)(2k-1)}{6}\right)+\left(72k+30\right)\left(\frac{k(k-1)}{2}\right)+(k-1)(24k-12)+48k-12\\
&= (24k^3-36k^2+12k)+(36k^3-21k^2-15k)+(24k^2-36k+12)+48k-12.
\end{aligned}
$$

Finally, $\forall k\in\mathbb{Z}$ the third Zagreb index is equal to

$$M_3(H_k)=60k^3-33k^2+9k.\blacksquare$$

4. CONCLUSION(S)

In Theoretical Chemistry, the topological indices and molecular structure descriptors are used for modeling physical-chemical, toxicological, biological and other properties of chemical compounds and nano structure analyzing.

In this paper, we were counting one of new molecular structure descriptors of Circumcoronene series of Benzenoid. The First eccentricity Zagreb index (third Zagreb index) $M^*_1(G)= M_3(G)=\sum_{uv\in E(G)} (ecc(v)+ecc(u))$ was introduced by *Ghorbani* and *Hosseinzadeh* in 2012. This new topological index is useful to surveying the structure of molecular graphs.

ACKNOWLEDGMENTS

The author is thankful to Professor Dr. *Mehdi Alaeiyan* from Department of Mathematics, Iran University of Science and Technology (IUST), and Professor Dr. *Mircea V. Diudea* from the Faculty of Chemistry and Chemical Engineering of Babes-Bolyai University (Romania) and *Dr. Miranda Petronella Vlad* from the Dimitrie Cantemir University, Bucharest, Faculty of Economic Sciences (Romania) for their precious support and suggestions

REFERENCES

1. I. Gutman, N. Trinajstić, Chem. Phys. Lett. 17 (1972) 535.
2. I. Gutman, K.C. Das. The first Zagreb index 30 years after. MATCH Commun. Math. Comput. Chem. 50 (2004) 83-92.
3. R. Todeschini and V. Consonni. Handbook of Molecular Descriptors. Wiley, Weinheim. (2000).
4. S. Nikolic, G. Kovacevic, A. Milicevic and N. Trinajstić. The Zagreb indices 30 years after, Croat. Chem. Acta 76 (2003) 113–124.

5. D. DeCaen, An upper bound on the sum of degrees in a graph. Discr. Math. 185 (1988) 245-248.
6. K.C. Das, Sharp bounds for the sum of the squares of the degrees of a graph, Kragujevac J. Math. 25 (2003) 31–49.
7. U.N. Peled, R. Petreschi and A. Sterbini, (n,e)-graphs with maximum sum of squares of degrees, J. Graph Theory 31 (1999) 283–295.
8. L.A. Szekely, L.H. Clark and R.C. Entringer, An inequality for degree sequences, Discr. Math., 103 (1992) 293–300.
9. M. Ghorbani and M.A. Hosseinzadeh, A New Version of Zagreb Indices, Filomat, 26(1) (2012) 93–100.
10. V. Sharma, R. Goswami, and A.K. Madan, Eccentric connectivity index: a novel highly of descriptor for structure-property and structure-activity studies, J. Chem. Inf. Comput. Sci. 37 (1997) 273-282.
11. S. Gupta, M. Singh, A.K. Madan, Connective eccentricity Index: A novel topological descriptor for predicting biological activity, J. Mol. Graph. Model. 18 (2000) 18- 25.
12. S. Gupta, M. Singh, A.K. Madan, Application of graph theory: Relationship of eccentric connectivity index and Wiener's index with anti-inammatory activity, J. Math. Anal. Appl. 266 (2002) 259-268.
13. S. Klavžar, I. Gutman and B. Mohar. Labeling of Benzenoid Systems which Reflects the Vertex-Distance Relations. J. Chem. Int Comput. Sci. 35 (1995) 590-593.
14. P. Zigert, S. Klavžar and I. Gutman. Calculating the hyper-Wiener index of benzenoid hydrocarbons. ACH Models Chem. 137 (2000) 83-94.
15. A. Soncini, E. Steiner, P.W. Fowler, R.W.A. Havenith, and L.W. Jenneskens. Perimeter Effects on Ring Currents in Polycyclic Aromatic Hydrocarbons, Circumcoronene and Two Hexabenzocoronenes. Chem. Eur. J. 9 (2003) 2974-2981.
16. P.E. John, P.V. Khadikar and J. Singh. A method of computing the PI index of benzenoid hydrocarbons using orthogonal cuts. J. Math. Chem. 42(1) (2007) 27-45.
17. S. Klavžar. A Bird's Eye View of The Cut Method and a Survey of Its Applications in Chemical Graph Theory. MATCH Commun. Math. Comput. Chem. 60 (2008) 255-274.
18. M.R. Farahani, Eccentricity Version of Atom-Bond Connectivity Index of Benzenoid Family $ABC_5(H_k)$. World Applied Sciences Journal 21(9) (2013) 1260-126.
19. M.R. Farahani, Computing a New Connectivity Index for a Famous Molecular Graph of Benzenoid Family. Journal of Chemica Acta 2 (2013) 26-31.
20. M.R. Farahani, The Ediz Eccentric Connectivity index and the Total Eccentricity Index of a Benzenoid System. Journal of Chemica Acta 2 (2013) 22-25.
21. M.R. Farahani. Computing Eccentricity Connectivity Polynomial of Circumcoronene Series of Benzenoid H_k by Ring-Cut Method. Annals of West University of Timisoara-Mathematics and Computer Science. 51(2) (2013) 29–37.
22. M.R. Farahani. Modified Eccentric Connectivity polynomial of Circumcoronene Series of Benzenoid H_k. Journal of Advances in Physics, 2(1) (2013) 48-52.
23. M.R. Farahani. Augmented Eccentric Connectivity Index of Molecular Graph. Int. J. Chem. Model. 6(1) (2014) 17-23.
24. M.R. Farahani. Zagreb index, Zagreb Polynomial of Circumcoronene Series of Benzenoid. Advances in Materials and Corrosion. 2 (2013) 16-19.